substrate according to the manufacturer's protocol except that a 10-fold higher substrate concentration was used (ViviRen Live Cell Substrate; Promega). The fluorescent and bioluminescent signals were measured using a Tristar LB941 (Berthold Technologies, Bad Wildbad, Germany).

Bimolecular fluorescence complementation–BRET analysis. 293T cells grown in a six-well plate were cotransfected with equal amounts of mKGN and mKGC (31.3–1000 ng) along with the Rluc constructs for CXCR4 or CXCR3 (20–200 ng). The BiFC–BRET signal was measured according to the BRET protocol described above.

Results

Establishment of the BRET system to measure molecular interactions. We used the BRET system to measure the homotypic interaction of CXCR4 (Fig. 2a). Wild-type CXCR4 was fused to either enhanced GFP or Rluc at its carboxy-terminus. Previous studies indicate that CXCR4 function is not affected by this modification.[31,34,35] The expression of CXCR4-GFP and CXCR4-Rluc were verified by western blot analysis using anti-GFP and anti-Rluc antibodies, confocal microscopy, flow cytometric analysis, and immunofluorescence analysis (Fig. 2b,c; data not shown). Two days after cotransfection of the CXCR4-GFP and CXCR4-Rluc expression plasmids into 293T cells, we incubated cells with the cell-permeable Rluc substrate and measured the GFP fluorescence, the net Rluc bioluminescence, and the bioluminescence through 485-nm (window A) and 525-nm (window B) emission filters. The BRET efficiency was defined as the ratio of the window B and window A values. As a positive control, we used the GFP-Rluc fusion protein that should theoretically have the best BRET efficiency. As a negative control, we cotransfected cells with GFP and Rluc expression plasmids. The average and standard deviation of BRET values between CXCR4-GFP and CXCR4-Rluc was 1.103 ± 0.160 where the negative and positive controls yielded 0.667 ± 0.084 and 1.444 ± 0.109, respectively (Table 1). The CXCR4 BRET signals were significantly higher than those of the negative control ($P < 0.001$, Student's t-test). Even the transfected cells expressed ~5–10-fold higher levels of GFP and Rluc in the negative control than did cells transfected with pCXCR4-GFP and pCXCR4-Rluc (data not shown).

The specificity of CXCR4-to-CXCR4 BRET signals has been a concern, as GPCR may yield non-specific BRET signals. To address this, we carried out out two experiments: a competition assay and a BRET measurement between heterologous chemokine receptors. The tripartite transfection of cells with pCXCR4, pCXCR4-GFP, and pCXCR4-Rluc resulted in a reduction of the BRET signal to 0.812 ± 0.058, which is significantly less than the BRET levels between CXCR4-GFP and CXCR4-Rluc ($P < 0.001$; Table 1). We defined the BRET level between GFP and Rluc as 0%, and that between CXCR4-GFP and CXCR4-Rluc as 100%, and used these normalized values to determine the relative BRET efficiency of each interaction. The presence of pCXCR4 reduced the BRET level to 39.3%, most likely because of the interference of the BRET-inducing homotypic CXCR4 interaction by untagged CXCR4.

We next examined various chemokine receptors, including CXCR2, CXCR3, and CCR5. Membrane targeting of these chemokine receptors was visualized by confocal microscopy (Fig. 2c), fluorescence activated cell sorting (FACS) analysis, and an immunofluorescence assay (data not shown). CXCR4-Rluc yielded low BRET signals (Table 1) with either membrane-targeted GFP (MEM-GFP; 0.609 ± 0.041, 0.0%), CXCR2-GFP (0.791 ± 0.093, 16.4%), CXCR3-GFP (0.718 ± 0.083, 7.9%), or CCR5-GFP (0.737 ± 0.057, 2.0%). Similar observations were made for the BRET signals between CXCR4-GFP and CXCR2-Rluc (0.762 ± 0.093, 10.2%) or CXCR4-GFP and CXCR3-Rluc (0.709 ± 0.064, 6.2%). These data suggest that the BRET assay detects specific homotypic interactions of CXCR4. Consistent with this, we also detected the homotypic interaction of CXCR4, but not the CXCR4–CXCR3 interaction, using a BiFC assay. Although some have suggested a possible homotypic interaction of CXCR2,[36] this interaction did not yield BRET signals as high as those with CXCR4 in our experimental set up, suggesting that the homotypic interaction of CXCR4 is substantially stronger than that of other chemokine receptors. Throughout this study, the BRET and BiFC assays were carried out under conditions where the transfected cells expressed similar levels of GFP and Rluc.

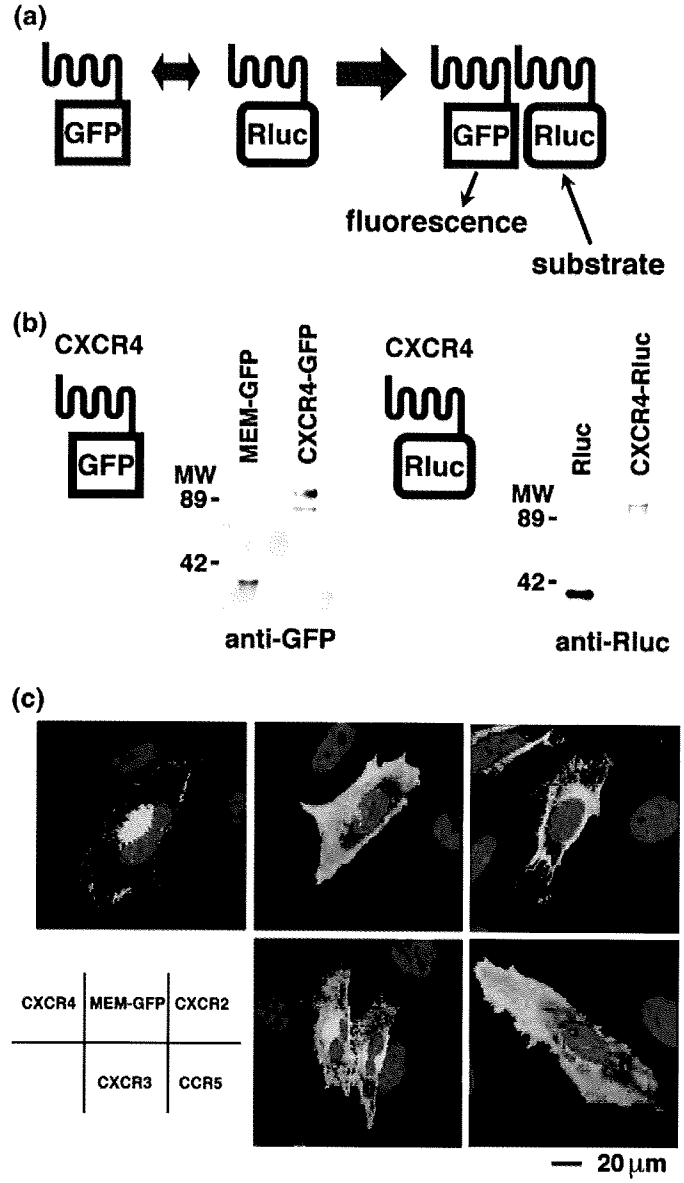

Fig. 2. Bioluminescent resonance energy transfer (BRET) assay to detect CXCR4 homotypic interactions. (a) Schematic drawing of the BRET assay system. The bioluminescence energy from renilla luciferase (Rluc) was absorbed by green fluorescent protein (GFP) to emit green fluorescence. (b) Detection of CXCR4-GFP and CXCR4-Rluc expression by western blotting. The GFP and Rluc fusion proteins were detected by anti-GFP and anti-Rluc antibodies, respectively. The molecular-weight markers are indicated on the left (kDa). (c) The intracellular distribution of CXCR4-GFP (top, left), MEM-GFP (top, middle), CXCR2-GFP (top, right), CXCR3-GFP (bottom, left), and CCR5-GFP (bottom, right). Green and blue represent GFP and the Hoechst 33258-stained nucleus, respectively. Magnification, ×630; scale bar = 20 μm.

Table 1. Detection of specific CXCR4–CXCR4 interactions by bioluminescent resonance energy transfer (BRET) analysis

Sample	BRET level†	*n*	*P*-value	Relative BRET efficiency (%)‡
GFP-Rluc fusion protein	1.444 ± 0.109	20	Not tested	–
GFP + Rluc	0.667 ± 0.084	21	Not tested	0.0
CXCR4-GFP + CXCR4-Rluc	1.103 ± 0.160	21	Not tested	100.0
CXCR4 FL-GFP + CXCR4-Rluc + CXCR4	0.812 ± 0.058	4	<0.001	39.3
MEM-GFP + CXCR4-Rluc	0.609 ± 0.041	5	<0.001	0.0
CXCR2-GFP + CXCR2-Rluc	0.784 ± 0.096	6	<0.001	13.0
CXCR2-GFP + CXCR4-Rluc	0.791 ± 0.093	6	<0.001	16.4
CXCR4-GFP + CXCR2-Rluc	0.762 ± 0.093	6	<0.001	10.2
CXCR3-GFP + CXCR3-Rluc	0.688 ± 0.060	6	<0.001	5.1
CXCR3-GFP + CXCR4-Rluc	0.718 ± 0.083	6	<0.001	7.9
CXCR4-GFP + CXCR3-Rluc	0.709 ± 0.064	6	<0.001	6.2
CCR5-GFP + CXCR4-Rluc	0.737 ± 0.057	4	<0.001	2.0

†The average and standard deviation of the indicated number of independent experiments.
The statistical significance of each BRET efficiency was tested compared to the BRET signal of CXCR4-GFP and CXCR4-Rluc (Student's *t*-test).
‡The relative BRET efficiency for each experiment was averaged.

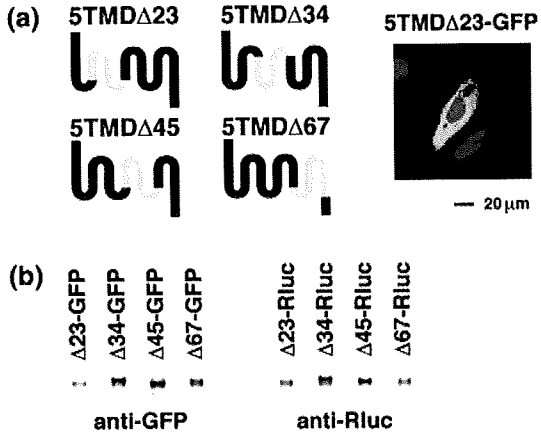

Fig. 3. Analyses of the transmembrane domain (TMD) mutants of CXCR4. (a) Schematic drawing of CXCR4 5TMD mutants. The deleted portions are indicated in gray. The intracellular distribution of 5TMDΔ23-GFP is shown as a representative. Green and blue represent green fluorescent protein (GFP) and the Hoechst 33258-stained nucleus, respectively. Magnification, ×630; scale bar = 20 μm. (b) Detection of CXCR4 5TMD-GFP and 5TMD-Rluc derivative expression by western blotting. The GFP and renilla luciferase (Rluc) fusion proteins were detected by anti-GFP and anti-Rluc antibodies, respectively.

Table 2. Detection of homotypic and heterotypic interactions between five transmembrane domain (5TMD) derivatives by bioluminescent resonance energy transfer (BRET) analysis

Sample	BRET level†	*n*	Relative BRET efficiency (%)‡
Homotypic interaction			
5TMDΔ23-GFP + 5TMDΔ23-Rluc	1.130 ± 0.091	7	115.7
5TMDΔ34-GFP + 5TMDΔ34-Rluc	1.209 ± 0.097	10	133.8
5TMDΔ45-GFP + 5TMDΔ45-Rluc	1.117 ± 0.095	7	112.6
5TMDΔ67-GFP + 5TMDΔ67-Rluc	1.102 ± 0.087	7	109.4
Heterotypic interaction			
5TMDΔ23-GFP + 5TMDΔ34-Rluc	1.060 ± 0.085	4	104.5
5TMDΔ23-GFP + 5TMDΔ45-Rluc	1.078 ± 0.093	3	112.7
5TMDΔ23-GFP + 5TMDΔ67-Rluc	0.978 ± 0.078	7	81.8
5TMDΔ34-GFP + 5TMDΔ23-Rluc	1.299 ± 0.077	3	161.0
5TMDΔ34-GFP + 5TMDΔ45-Rluc	1.177 ± 0.091	3	129.7
5TMDΔ34-GFP + 5TMDΔ67-Rluc	1.225 ± 0.105	3	141.3
5TMDΔ45-GFP + 5TMDΔ23-Rluc	1.080 ± 0.108	8	105.5
5TMDΔ45-GFP + 5TMDΔ34-Rluc	1.131 ± 0.050	4	121.5
5TMDΔ45-GFP + 5TMDΔ67-Rluc	1.161 ± 0.069	3	133.7
5TMDΔ67-GFP + 5TMDΔ23-Rluc	1.072 ± 0.096	3	111.3
5TMDΔ67-GFP + 5TMDΔ34-Rluc	1.065 ± 0.088	4	104.8
5TMDΔ67-GFP + 5TMDΔ45-Rluc	1.042 ± 0.094	3	104.0

†The average and standard deviation for the indicated number of independent experiments.
The statistical significance of each BRET efficiency was tested compared to the BRET signal of CXCR4-GFP and CXCR4-Rluc (Student's *t*-test). All were found to be not significant.
‡The relative BRET efficiency was calculated for each experiment and the average is shown.

Measuring the interaction between CXCR4 mutants carrying five TMD. The dimerization model predicts the presence of a CXCR4 mutant defective in the homotypic interaction. To map the domains required for the homotypic interaction of CXCR4, we constructed a series of deletion mutants. It has been reported that removing two transmembrane domains alters neither the membrane topology nor the functions of CXCR4.[37] Thus, we constructed four mutants, 5TMDΔ23, 5TMDΔ34, 5TMDΔ45, and 5TMDΔ67, and fused these mutants to either GFP or Rluc at their carboxy-termini (Fig. 3a). The expression of the 5TMD derivatives was verified by western blot analysis (Fig. 3b). The intracellular distribution of 5TMDD23-GFP was mostly cytoplasmic with reticular patterns (Fig. 3a), and all 5TMD-GFP derivatives showed similar distributions. The BRET efficiencies of homotypic pairs of GFP- and Rluc-tagged 5TMD derivatives were comparable to those of full-length CXCR4 (109.4–133.8%; Table 2). Furthermore, any pair of 5TMD derivatives yielded BRET signal levels similar to those of CXCR4-GFP and CXCR4-Rluc (81.8–161.0%; Table 2). None of the combinations yielded significantly lower BRET signals than the full-length CXCR4 combination. These data suggest that either: (1) the interactions between the 5TMD mutants are mediated by the amino- or caroboxy-termini, or the first TMD, as these are shared by all of the 5TMD derivatives; or (2) there are more than two interaction facets in CXCR4, which would make interactions between any two of the 5TMD mutants possible.

Contribution of the amino- or carboxy-terminal domains and the first TMD to CXCR4 oligomerization. To differentiate between the above possibilities, we assessed the potential contribution of the extracellular amino-terminal and the cytoplasmic carboxy-terminal domains to CXCR4 oligomerization. We used a CXCR2–CXCR4 chimeric construct, CXCR2/4, which has the amino-terminus of CXCR2 fused to the first TMD of CXCR4 (Fig. 4a). CXCR2/4 is

doi: 10.1111/j.1349-7006.2008.00997.x

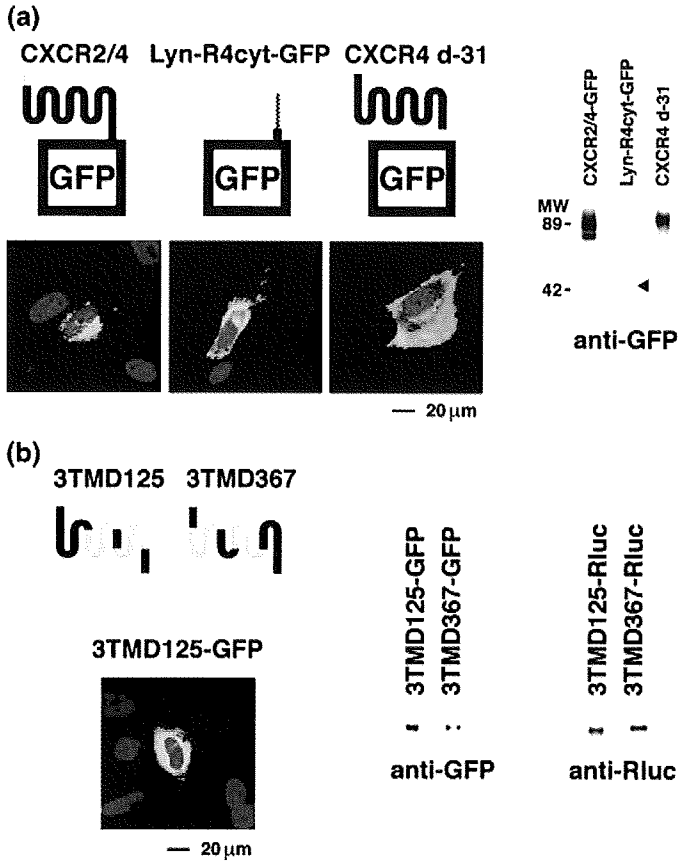

Fig. 4. Assessment of the relative contribution of the CXCR4 amino- and carboxy-termini and the first transmembrane domain (TMD) to oligomerization. (a) Schematic drawing of CXCR2/4-GFP (left), Lyn-R4cyt-GFP (middle), and CXCR4 d-31 (right). The substituted or deleted regions are indicated in gray. The intracellular distribution of each construct is shown. Protein expression was detected by anti-GFP antibody (Lyn-R4cyt-GFP, arrowhead). The molecular-weight markers are indicated on the left (kDa). (b) Schematic drawing of the CXCR4 3TMD mutants. The deleted portions are indicated in gray. The green fluorescent protein (GFP) and renilla luciferase (Rluc) fusion proteins were detected by anti-GFP and anti-Rluc antibodies, respectively. The intracellular distribution of 3TMD125-GFP is shown as a representative. Green and blue represent GFP and the Hoechst 33258-stained nucleus, respectively. Magnification, ×630; scale bar = 20 μm.

known to support HIV-1 entry and CXCL12/SDF-1α signaling.[32,38] The intracellular distribution of CXCR2/4-GFP was similar to that of CXCR4-GFP (Fig. 4a). The interaction between CXCR2/4-GFP and CXCR4-Rluc yielded the BRET signal (to 1.163 ± 0.106, 71.9%; Table 3), which was not significantly different from the BRET levels of CXCR4-GFP and CXCR4-Rluc. Given that only a low BRET signal was detected between CXCR2 and CXCR4 in these experimental conditions (Table 1), this suggests that the amino-terminus of CXCR4 contributes little to its oligomerization.

We next investigated the cytoplasmic tail of CXCR4. The amino-terminus of the CXCR4 cytoplasmic domain was fused to the myristoylation signal motif of *lyn* and the carboxy-terminus was fused to GFP (Lyn-R4cyt-GFP), thereby allowing the cytoplasmic domain of CXCR4 to target the plasma membrane in a native membrane topology (Fig. 4a). As expected, Lyn-R4cyt-GFP was distributed to the plasma membrane, as indicated by microscopic observation (Fig. 4a). However, the BRET signal between Lyn-R4cyt-GFP and CXCR4-Rluc was not detected (0.758 ± 0.057, 4.8%; Table 3). We also tested the cytoplasmic tail-deleted mutant of CXCR4 (Fig. 4a). By removing the cytoplasmic tail of CXCR4, it lost its ability to signal upon ligand binding, but retained its HIV-1 coreceptor function.[32,38] When the carboxy-terminal 31 amino acids were removed (CXCR4 d-31), the BRET signal between CXCR4 d-31-GFP and CXCR4-Rluc was 1.111 ± 0.083 (98.9%), which is comparable to levels seen with the homotypic interaction of full-length CXCR4 (Table 3). These data suggest that CXCR4 oligomerization is not mediated by the amino- or carboxy-termini, but mainly by TMD.

Finally, to examine the possible role of the first TMD in CXCR4 oligomerization, we constructed two CXCR4 mutants carrying three TMD. The 3TMD125 and 3TMD367 mutants have the first, second, and fifth, or the third, sixth, and seventh TMD, respectively, and both were fused to either GFP or Rluc (Fig. 4b). The intracellular distribution of 3TMD-GFP derivatives was similar to those of the 5TMD-GFP derivatives (3TMD125-GFP in Fig. 4b). If the first TMD plays a major role in CXCR4 oligomerization, the BRET signal between 3TMD125-GFP and 3TMD125-Rluc derivatives should be higher than that between 3TMD367 derivatives. Furthermore, if the dimerization model is correct, then the 3TMD125 and 3TMD367 derivatives should not yield detectable BRET signals as they do not share any TMD. We found that the BRET signal representing the homotypic interaction of 3TMD125 was 0.806 ± 0.071 (30.8%), which was significantly higher than the negative control ($P < 0.01$) but lower than that of 3TMD367 (0.917 ± 0.061, 64.0%, $P < 0.05$; Table 3). These data are not consistent with the dimerization model, suggesting that the contribution of the first TMD to the homotypic CXCR4 interaction is relatively small.

The heterotypic interactions between 3TMD and 5TMD derivatives were also tested by the BRET assay. The 3TMD and 5TMD combinations yielded BRET signals that were significantly higher than the 3TMD combinations (72.0 ± 17.5 vs 51.5 ± 16.2%, $P < 0.05$; Table 3) but lower than the 5TMD pairs (72.0 ± 17.5 vs 117.7 ± 18.7%, $P < 0.001$; Tables 2,3). The observations that any pair of 5TMD mutants yielded BRET signals that were comparable to those of CXCR4, and that the BRET signals increased in parallel to the number of TMD, do not agree with a dimerization model and instead favor a multimerization model.

Detecting a higher-order oligomerization of CXCR4 with the BiFC–BRET system. We used the BiFC–BRET technique to directly demonstrate the presence of a trimolecular complex *in vivo*.[39] BiFC uses a 'split' GFP that fluoresces only when the amino- and carboxy-terminal fragments are forced into close proximity. When the BiFC assay is built into the BRET system, the BRET signal should be detected only when three molecules assemble, that is, proteins carrying Rluc and the amino- or carboxy-terminal fragments of GFP (Fig. 5a). We used monomeric mKG as a GFP.[40] The expression vectors of CXCR4 fused to the mKG amino- and carboxy-terminal fragments (mKGN and mKGC, respectively) were constructed. For controls, we constructed CXCR3-mKGN and CXCR3-mKGC. The expression of fusion proteins was verified by immunofluorescence analysis (Fig. 5b) and flow cytometric analysis (data not shown).

We detected BiFC signals when CXCR4-mKGN and CXCR4-mKGC were coexpressed, but not when either was expressed alone or when a pair of CXCR4 and CXCR3 derivatives were coexpressed, confirming the specificity of the BiFC analysis and the BRET results (Fig. 5b; Table 4). We considered the combination of CXCR4-mKGN, CXCR4-mKGC, and Rluc as a negative control. When increasing amounts of pCXCR4-mKGN and pCXCR4-mKGC were transfected into 293T cells along with pCXCR4-hRluc, we detected increasing BiFC–BRET signals that were significantly higher than the negative control (Table 4). Such high BiFC–BRET signals were not observed by tripartite transfection of plasmids expressing CXCR4-mKGN, CXCR4-mKGC, and CXCR3-Rluc, CXCR3-mKGN, CXCR3-mKGC, and CXCR4-Rluc, or CXCR4-mKGN, CXCR4-mKGC, and Rluc

Table 3. Contribution of the amino- and carboxy-terminal domains, and the first transmembrane domain (TMD) to CXCR4 oligomerization as analyzed by bioluminescent resonance energy transfer (BRET) analysis

Sample	BRET level[†]	*n*	*P*-value	Relative BRET efficiency (%)[‡]
Amino- and carboxy-terminal domain				
CXCR2/4-GFP + CXCR4-Rluc	1.163 ± 0.106	6	n.s.	71.9
Lyn My-R4cyt-GFP + CXCR4-Rluc	0.758 ± 0.057	4	<0.001	4.8
CXCR4 d-31-GFP + CXCR4-Rluc	1.111 ± 0.083	8	n.s.	98.9
3TMD homotypic interaction				
3TMD125-GFP + 3TMD125-Rluc	0.806 ± 0.071	5	<0.001	30.8
3TMD367-GFP + 3TMD367-Rluc	0.917 ± 0.061	6	<0.01	64.0
3TMDs heterotypic interaction				
3TMD125-GFP + 3TMD367-Rluc	0.806 ± 0.010	3	<0.001	46.3
3TMD367-GFP + 3TMD125-Rluc	0.885 ± 0.012	3	<0.05	64.7
3TMD–5TMD interaction				
5TMDΔ23-GFP + 3TMD125-Rluc	0.776 ± 0.020	4	<0.001	48.3
5TMDΔ23-GFP + 3TMD367-Rluc	0.877 ± 0.030	4	<0.01	73.3
5TMDΔ34-GFP + 3TMD125-Rluc	0.914 ± 0.041	4	<0.05	79.8
5TMDΔ34-GFP + 3TMD367-Rluc	1.009 ± 0.061	4	n.s.	103.0
5TMDΔ45-GFP + 3TMD125-Rluc	0.931 ± 0.024	4	<0.05	84.5
5TMDΔ45-GFP + 3TMD367-Rluc	0.937 ± 0.010	4	n.s.	86.5
5TMDΔ67-GFP + 3TMD125-Rluc	0.826 ± 0.031	4	<0.01	59.5
5TMDΔ67-GFP + 3TMD367-Rluc	0.892 ± 0.011	4	<0.05	75.8
3TMD125-GFP + 5TMDΔ23-Rluc	0.841 ± 0.088	4	<0.01	57.3
3TMD125-GFP + 5TMDΔ34-Rluc	0.819 ± 0.044	4	<0.01	52.8
3TMD125-GFP + 5TMDΔ45-Rluc	0.846 ± 0.049	4	<0.01	58.3
3TMD125-GFP + 5TMDΔ67-Rluc	0.824 ± 0.061	4	<0.01	53.0
3TMD367-GFP + 5TMDΔ23-Rluc	0.990 ± 0.041	5	n.s.	91.8
3TMD367-GFP + 5TMDΔ34-Rluc	0.989 ± 0.028	4	n.s.	93.8
3TMD367-GFP + 5TMDΔ45-Rluc	0.958 ± 0.042	4	n.s.	85.5
3TMD367-GFP + 5TMDΔ67-Rluc	0.984 ± 0.053	4	n.s.	91.8

[†]The average and standard deviation for the indicated number of independent experiments.
The statistical significance of each BRET efficiency was tested compared to the BRET signal of CXCR4-GFP and CXCR4-Rluc (Student's *t*-test). n.s., not significant.
[‡]The relative BRET efficiency was calculated for each experiment and the average is shown.

Table 4. Detection of higher-order multimerization of CXCR4 by bioluminescent resonance energy transfer (BRET)–bimolecular fluorescence complementation (BiFC) analysis

Sample	BiFC–BRET signal[†]	*n*	*P*-value
Specificity control			
mKGN 1000 ng + mKGC 1000 ng + Rluc	0.615 ± 0.070	3	
CXCR4 mKGN 500 ng + CXCR4 mKGC 500 ng + Rluc	0.624 ± 0.049	6	
CXCR3 mKGN 1000 ng + CXCR3 mKGC 1000 ng + CXCR3 Rluc	0.569 ± 0.021	3	
CXCR4–CXCR3 interaction			
CXCR3 mKGN 1000 ng + CXCR3 mKGC 1000 ng + CXCR4 Rluc	0.610 ± 0.065	3	n.s.
CXCR4 mKGN 31.3 ng + CXCR4 mKGC 31.3 ng + CXCR3 Rluc	0.593 ± 0.021	4	n.s.
CXCR4 mKGN 62.5 ng + CXCR4 mKGC 62.5 ng + CXCR3 Rluc	0.582 ± 0.011	4	n.s.
CXCR4 mKGN 125 ng + CXCR4 mKGC 125 ng + CXCR3 Rluc	0.586 ± 0.015	4	n.s.
CXCR4 mKGN 250 ng + CXCR4 mKGC 250 ng + CXCR3 Rluc	0.568 ± 0.011	4	n.s.
CXCR4 mKGN 500 ng + CXCR4 mKGC 500 ng + CXCR3 Rluc	0.573 ± 0.014	4	n.s.
CXCR4–CXCR4 interaction			
CXCR4 mKGN 31.3 ng + CXCR4 mKGC 31.3 ng + CXCR4 Rluc	0.634 ± 0.023	6	n.s.
CXCR4 mKGN 62.5 ng + CXCR4 mKGC 62.5 ng + CXCR4 Rluc	0.644 ± 0.035	7	n.s.
CXCR4 mKGN 125 ng + CXCR4 mKGC 125 ng + CXCR4 Rluc	0.676 ± 0.016	7	<0.05
CXCR4 mKGN 250 ng + CXCR4 mKGC 250 ng + CXCR4 Rluc	0.707 ± 0.030	7	<0.01
CXCR4 mKGN 500 ng + CXCR4 mKGC 500 ng + CXCR4 Rluc	0.717 ± 0.054	10	<0.01

[†]The average and standard deviation for the indicated number of independent experiments are shown.
The statistical significance of each BiFC–BRET signal was tested compared to the signal of CXCR4 mKGN + CXCR4 mKGC + Rluc (Student's *t*-test). n.s., not significant. The gray scale code represents the BRET efficiency: >100%, black; >80% dark gray; >60%, gray; >40%, light gray; >20%, white gray; <20%, white.

doi: 10.1111/j.1349-7006.2008.00997.x

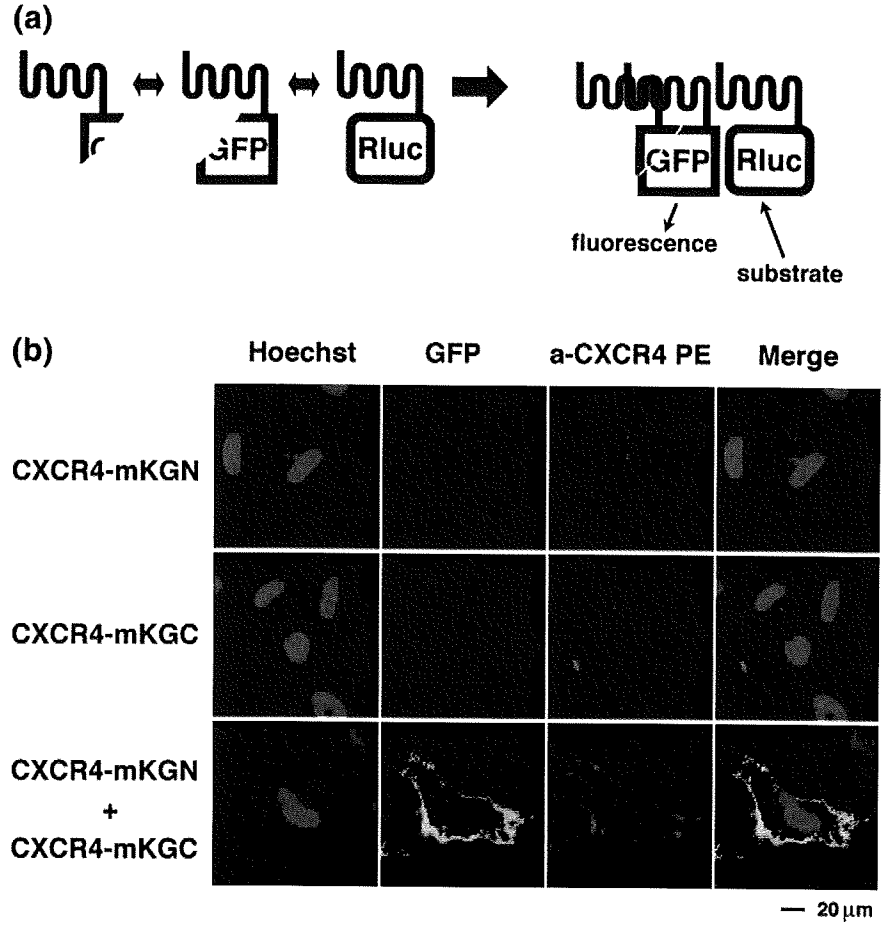

Fig. 5. Bioluminescent resonance energy transfer (BRET)–bimolecular fluorescence complementation (BiFC) analysis to demonstrate the presence of a higher-order molecular clustering of CXCR4. (a) Schematic drawing of the BiFC–BRET assay system. The bioluminescence energy from renilla luciferase (Rluc) was absorbed by green fluorescent protein (GFP; mKG) reconstituted by amino- and carboxy-terminal fragments to emit green fluorescence. (b) Detection of a BiFC signal by coexpressing CXCR4-mKGN and CXCR-mKGC. Cell surface expression of CXCR4-mKGN and CXCR4-mKGC was detected by an immunofluorescence assay using anti-CXCR4 R-phycoerythrin (PE) (a-CXCR4 R-phycoerythrin). The green fluorescence was detected only when two constructs were cointroduced into cells (bottom). Green, red, and blue represent GFP, PE, and the Hoechst 33258-stained nucleus, respectively. Magnification, ×630; scale bar = 20 μm.

(Table 4). These data indicate that the BiFC–BRET signal is specific for CXCR4, and that CXCR4 forms a molecular complex consisting of more than two molecules *in vivo*. The BiFC–BRET signals were lower than the BRET signals, presumably because of the decreased efficiencies of green fluorescence activation by mKGN and mKGC fragments relative to full-length GFP. Taken together, our *in vivo* biophysical analysis favors a multimerization model for CXCR4.

Discussion

In the present work, we demonstrated that CXCR4 forms a complex consisting of more than two molecules (a multimer) in the absence of CXCL12/SDF-1α by using a combination of BRET and BiFC techniques. The BiFC–BRET approach is a powerful technique for directly identifying a trimolecular complex in living cells, and may be applied to other protein–protein interactions.

Any application of FRET or BRET techniques to GPCR has to be done carefully, as GPCR often yield significant background signals.[41] The use of comparative studies with other GPCR, including CXCR2, CXCR3, and CCR5, as well as the careful monitoring of GFP and Rluc expression levels, allowed us to obtain compelling evidence for a specific homotypic interaction of CXCR4. The technical limitation of BiFC–BRET is that it is not possible to determine how many molecules are involved in the higher-order complex. To further characterize the molecular assembly, it will be necessary to develop a system that yields signals only when a target molecule tetramerizes.

We demonstrated that the higher-order clusterization of CXCR4 was not mediated by the amino- or carboxy-termini but by multiple TMD, consistent with the GPCR oligomerization models. However, we were unable to determine the TMD pairs that contribute most to CXCR4 multimerization. Consequently, we failed to isolate monomeric CXCR4. Treating cells with the CXCR4 ligand CXCL12/SDF-1α at cell migration-inducing concentrations did not increase BRET levels (data not shown), also suggesting the presence of higher-order CXCR4 clusters under steady-state conditions. This type of preformed receptor multimerization has been documented for receptors such as CCR5.[28] The biological advantage of CXCR4 assembly is its effective ability to 'radar' CXCL12/SDF-1α in the microenvironment for the induction of cell migration or targeted metastasis of cancer cells.[42,43] Steady-state multimerization is important because a molecular cluster would increase avidity for CXCL12/SDF-1α. We assume that high sensitivity for the ligand is critical for normal and malignant cells to be able to determine which direction to migrate to in in response to ligand stimulation.

CXCR4 does not display apparent punctate signals on the cell surface, as visualized by GFP tagging or immunostaining, even though our data predict that CXCR4 multimerizes. This suggests that only a limited number of CXCR4 molecules might participate in a multimeric unit. Bovine rhodopsin has been demonstrated to form a higher-order structure characterized by dimer arrays.[44] Given the structural similarities among GPCR, the basic unit of the higher-order cluster of CXCR4 may also be a dimer. It is possible that a pair of dimers forms a CXCR4 tetramolecular complex. These hypothetical models may be probed further using atomic force microscopy.

As shown in Figure 5b, the expression of CXCR4-mKGN and CXCR4-mKGC yielded green fluorescence at the cell periphery. This is compelling evidence that CXCR4 multimerizes at the cell surface. CXCR4 does not actively form a complex in the ER

but does so in the post-ER-to-Golgi compartments as suggested by the following data. When 293T cells expressing CXCR4-GFP and CXCR4-Rluc were treated with brefeldin A, which blocks the transport of proteins from the ER to post-Golgi compartments, the BRET levels dropped substantially to $63.7 \pm 15.2\%$ ($n = 7$) at 4 h after exposure. This drop in BRET level corresponded to the decrease in cell surface CXCR4 levels, even though the GFP and Rluc levels were unchanged (data not shown). Thus, it is unlikely that multimerization is required for CXCR4 to egress from the ER. CXCR4 may start to oligomerize in post-ER compartments and probably play a role at the cell surface, as hypothesized above. We believe that it will be informative to study how CXCR4 oligomerization is prohibited in the ER. By knowing this, we may be able to design novel CXCR4 inhibitors that disassemble the CXCR4 multimer. BiFC–BRET-based biophysical analyses would be a powerful tool for further studies.

Acknowledgments

We thank Dr Tsutomu Murakami for critically reading the manuscript. This work was partly supported by the Japan Health Science Foundation, the Japanese Ministry of Health, Labor and Welfare (H18-AIDS-W-003), and the Japanese Ministry of Education, Culture, Sports, Science, and Technology (18689014 and 18659136).

References

1 Gupta SK, Lysko PG, Pillarisetti K *et al.* Chemokine receptors in human endothelial cells. Functional expression of CXCR4 and its transcriptional regulation by inflammatory cytokines. *J Biol Chem* 1998; **273**: 4282–7.
2 Li S, Huang S, Peng SB. Overexpression of G protein-coupled receptors in cancer cells: involvement in tumor progression. *Int J Oncol* 2005; **27**: 1329–39.
3 Balabanian K, Lagane B, Pablos JL *et al.* WHIM syndromes with different genetic anomalies are accounted for by impaired CXCR4 desensitization to CXCL12. *Blood* 2005; **105**: 2449–57.
4 Gulino AV, Moratto D, Sozzani S *et al.* Altered leukocyte response to CXCL12 in patients with warts hypogammaglobulinemia, infections, myelokathexis (WHIM) syndrome. *Blood* 2004; **104**: 444–52.
5 Hernandez PA, Gorlin RJ, Lukens JN *et al.* Mutations in the chemokine receptor gene *CXCR4* are associated with WHIM syndrome, a combined immunodeficiency disease. *Nat Genet* 2003; **34**: 70–4.
6 Zou YR, Kottmann AH, Kuroda M, Taniuchi I, Littman DR. Function of the chemokine receptor CXCR4 in haematopoiesis and in cerebellar development. *Nature* 1998; **393**: 595–9.
7 Feng Y, Broder CC, Kennedy PE, Berger EA. HIV-1 entry cofactor: functional cDNA cloning of a seven-transmembrane, G protein-coupled receptor. *Science* 1996; **272**: 872–7.
8 Koizumi K, Hojo S, Akashi T, Yasumoto K, Saiki I. Chemokine receptors in cancer metastasis and cancer cell-derived chemokines in host immune response. *Cancer Sci* 2007; **98**: 1652–8.
9 Arya M, Ahmed H, Silhi N, Williamson M, Patel HR. Clinical importance and therapeutic implications of the pivotal CXCL12–CXCR4 (chemokine ligand–receptor) interaction in cancer cell migration. *Tumour Biol* 2007; **28**: 123–31.
10 Raman D, Baugher PJ, Thu YM, Richmond A. Role of chemokines in tumor growth. *Cancer Lett* 2007; **256**: 137–65.
11 Billadeau DD, Chatterjee S, Bramati P *et al.* Characterization of the CXCR4 signaling in pancreatic cancer cells. *Int J Gastrointest Cancer* 2006; **37**: 110–19.
12 Akashi T, Koizumi K, Tsuneyama K, Saiki I, Takano Y, Fuse H. Chemokine receptor CXCR4 expression and prognosis in patients with metastatic prostate cancer. *Cancer Sci* 2008; **99**: 539–42.
13 Yang S, Pham LK, Liao CP, Frenkel B, Reddi AH, Roy-Burman P. A novel bone morphogenetic protein signaling in heterotypic cell interactions in prostate cancer. *Cancer Res* 2008; **68**: 198–205.
14 De Falco V, Guarino V, Avilla E *et al.* Biological role and potential therapeutic targeting of the chemokine receptor CXCR4 in undifferentiated thyroid cancer. *Cancer Res* 2007; **67**: 11 821–9.
15 Tucci MG, Lucarini G, Brancorsini D *et al.* Involvement of E-cadherin, beta-catenin, Cdc42 and CXCR4 in the progression and prognosis of cutaneous melanoma. *Br J Dermatol* 2007; **157**: 1212–16.
16 Kollmar O, Rupertus K, Scheuer C *et al.* Stromal cell-derived factor-1 promotes cell migration and tumor growth of colorectal metastasis. *Neoplasia* 2007; **9**: 862–70.
17 Holmes WD, Consler TG, Dallas WS, Rocque WJ, Willard DH. Solution studies of recombinant human stromal-cell-derived factor-1. *Protein Expr Purif* 2001; **21**: 367–77.
18 Veldkamp CT, Peterson FC, Pelzek AJ, Volkman BF. The monomer–dimer equilibrium of stromal cell-derived factor-1 (CXCL 12) is altered by pH, phosphate, sulfate, and heparin. *Protein Sci* 2005; **14**: 1071–81.
19 Baryshnikova OK, Sykes BD. Backbone dynamics of SDF-1α determined by NMR: interpretation in the presence of monomer–dimer equilibrium. *Protein Sci* 2006; **15**: 2568–78.
20 Babcock GJ, Farzan M, Sodroski J. Ligand-independent dimerization of CXCR4, a principal HIV-1 coreceptor. *J Biol Chem* 2003; **278**: 3378–85.
21 Vila-Coro AJ, Rodriguez-Frade JM, Martin De Ana A, Moreno-Ortiz MC, Martinez AC, Mellado M. The chemokine SDF-1α triggers CXCR4 receptor dimerization and activates the JAK/STAT pathway. *FASEB J* 1999; **13**: 1699–710.
22 Toth PT, Ren D, Miller RJ. Regulation of CXCR4 receptor dimerization by the chemokine SDF-1α and the HIV-1 coat protein gp120: a fluorescence resonance energy transfer (FRET) study. *J Pharmacol Exp Ther* 2004; **310**: 8–17.
23 Wang J, He L, Combs CA, Roderiquez G, Norcross MA. Dimerization of CXCR4 in living malignant cells: control of cell migration by a synthetic peptide that reduces homologous CXCR4 interactions. *Mol Cancer Ther* 2006; **5**: 2474–83.
24 Terrillon S, Bouvier M. Roles of G-protein-coupled receptor dimerization. *EMBO Rep* 2004; **5**: 30–4.
25 Milligan G. G protein-coupled receptor dimerization: function and ligand pharmacology. *Mol Pharmacol* 2004; **66**: 1–7.
26 Lee SP, O'Dowd BF, Rajaram RD, Nguyen T, George SR. D2 dopamine receptor homodimerization is mediated by multiple sites of interaction, including an intermolecular interaction involving transmembrane domain 4. *Biochemistry* 2003; **42**: 11 023–31.
27 Thevenin D, Lazarova T, Roberts MF, Robinson CR. Oligomerization of the fifth transmembrane domain from the adenosine A2A receptor. *Protein Sci* 2005; **14**: 2177–86.
28 Hernanz-Falcon P, Rodriguez-Frade JM, Serrano A *et al.* Identification of amino acid residues crucial for chemokine receptor dimerization. *Nat Immunol* 2004; **5**: 216–23.
29 Muller-Taubenberger A, Anderson KI. Recent advances using green and red fluorescent protein variants. *Appl Microbiol Biotechnol* 2007; **77**: 1–12.
30 Gandia J, Galino J, Amaral OB *et al.* Detection of higher-order G protein-coupled receptor oligomers by a combined BRET–BiFC technique. *FEBS Lett* 2008; **582**: 2979–84.
31 Futahashi Y, Komano J, Urano E *et al.* Separate elements are required for ligand-dependent and -independent internalization of metastatic potentiator CXCR4. *Cancer Sci* 2007; **98**: 373–9.
32 Doranz BJ, Orsini MJ, Turner JD *et al.* Identification of CXCR4 domains that support coreceptor and chemokine receptor functions. *J Virol* 1999; **73**: 2752–61.
33 Shimizu S, Urano E, Futahashi Y *et al.* Inhibiting lentiviral replication by HEXIM1, a cellular negative regulator of the CDK9/cyclin T complex. *AIDS* 2007; **21**: 575–82.
34 Tarasova NI, Stauber RH, Michejda CJ. Spontaneous and ligand-induced trafficking of CXC-chemokine receptor 4. *J Biol Chem* 1998; **273**: 15 883–6.
35 Gether U. Uncovering molecular mechanisms involved in activation of G protein-coupled receptors. *Endocr Rev* 2000; **21**: 90–113.
36 Trettel F, Di Bartolomeo S, Lauro C, Catalano M, Ciotti MT, Limatola C. Ligand-independent CXCR2 dimerization. *J Biol Chem* 2003; **278**: 40 980–8.
37 Ling K, Wang P, Zhao J *et al.* Five-transmembrane domains appear sufficient for a G protein-coupled receptor: functional five-transmembrane domain chemokine receptors. *Proc Natl Acad Sci USA* 1999; **96**: 7922–7.
38 Willett BJ, Adema K, Heveker N *et al.* The second extracellular loop of CXCR4 determines its function as a receptor for feline immunodeficiency virus. *J Virol* 1998; **72**: 6475–81.
39 Heroux M, Hogue M, Lemieux S, Bouvier M. Functional calcitonin gene-related peptide receptors are formed by the asymmetric assembly of a calcitonin receptor-like receptor homo-oligomer and a monomer of receptor activity-modifying protein-1. *J Biol Chem* 2007; **282**: 31 610–20.
40 Ip DT, Wong KB, Wan DC. Characterization of novel orange fluorescent protein cloned from cnidarian tube anemone *Cerianthus* sp. *Mar Biotechnol (NY)* 2007; **9**: 469–78.
41 Salahpour A, Masri B. Experimental challenge to a 'rigorous' BRET analysis of GPCR oligomerization. *Nat Meth* 2007; **4**: 599–600.
42 Wang J, Loberg R, Taichman RS. The pivotal role of CXCL12 (SDF-1)/CXCR4 axis in bone metastasis. *Cancer Metastasis Rev* 2006; **25**: 573–87.
43 Burger JA, Kipps TJ. CXCR4: a key receptor in the crosstalk between tumor cells and their microenvironment. *Blood* 2006; **107**: 1761–7.
44 Fotiadis D, Liang Y, Filipek S, Saperstein DA, Engel A, Palczewski K. Atomic-force microscopy: Rhodopsin dimers in native disc membranes. *Nature* 2003; **421**: 127–8.

doi: 10.1111/j.1349-7006.2008.00997.x

Dominant-negative derivative of EBNA1 represses EBNA1-mediated transforming gene expression during the acute phase of Epstein–Barr virus infection independent of rapid loss of viral genome

Yumi Kariya,[1,2] Makiko Hamatake,[1] Emiko Urano,[1] Hironori Yoshiyama,[3] Norio Shimizu[2] and Jun Komano[1,4]

[1]AIDS Research Center, National Institute of Infectious Diseases, Tokyo; [2]Department of Virology, Division of Medical Science, Medical Research Institute, Tokyo Medical and Dental University, Tokyo; [3]Research Center for Infection-associated Cancer, Institute for Genetic Medicine, Hokkaido University, Sapporo, Japan

(Received November 1, 2009/Revised November 30, 2009/Accepted December 6, 2009)

The oncogenic human herpes virus, the Epstein–Barr virus (EBV), expresses EBNA1 in almost all forms of viral latency. EBNA1 plays a major role in the maintenance of the viral genome and in the transactivation of viral transforming genes, including EBNA2 and latent membrane protein (LMP-1). However, it is unknown whether inhibition of EBNA1 from the onset of EBV infection disrupts the establishment of EBV's latency and transactivation of the viral oncogenes. To address this, we measured EBV infection kinetics in the B cell lines BALL-1 and BJAB, which stably express a dominant-negative EBNA1 (dnE1) fused to green fluorescent protein (GFP). The EBV genome was surprisingly unstable 1 week post-infection: the average loss rate of EBV DNA from GFP- and GFP-dnE1-expressing cells was 53.4% and 41.0% per cell generation, respectively, which was substantially higher than that of an 'established' *oriP* replicon (2–4%). GFP-dnE1 did not accelerate loss of the EBV genome, suggesting that EBNA1-dependent licensing of the EBV genome occurs infrequently during the acute phase of EBV infection. In the subacute phase, establishment of EBV latency was completely blocked in GFP-dnE1-expressing cells. In contrast, C/W promoter-driven transcription was strongly restricted in GFP-dnE1-expressing cells at 2 days post-infection. These data suggest that inhibition of EBNA1 from the onset of EBV infection is effective in blocking the positive feedback loop in the transactivation of viral transforming genes, and in eradicating the EBV genome during the subacute phase. Our results suggest that gene transduction of GFP-dnE1 could be a promising therapeutic and prophylactic approach toward EBV-associated malignancies. (*Cancer Sci* 2010)

The Epstein–Barr virus (EBV) is a risk factor in several malignant diseases including Burkitt's lymphoma and nasopharyngeal carcinoma.[1–4] The opportunistic B-cell lymphoma is becoming the major cause of death in AIDS patients in an era of highly active antiretroviral therapy (HAART), and EBV is associated with a significant portion of AIDS lymphoma cases.[5,6] Neither an EBV vaccine, nor specific antiviral agents against EBV are available; thus attention should be paid to the development of therapeutic agents against EBV.

EBV-encoded genes including EBNA1, EBNA2, and latent membrane protein (LMP-1) are potential molecular targets for the treatment of EBV-associated lymphomas because they play central roles in the process of malignant transformation.[7] We are interested in EBNA1 since it contributes to EBV oncogenesis in two ways: it supports the maintenance of the EBV genome in *cis* and enhances expression of viral oncogenes, including EBNA2 and LMP-1, in *trans*.[7–9] EBNA1 exerts its biological functions by binding to its cognate binding sites within the family of repeats (FR) and the dyad symmetry element (DS) located within the origin of replication (oriP) of EBV DNA. EBNA1 interacts with FR to enhance transcription from the viral C/W promoters (C/Wp) and to partition EBV DNA to daughter cells; and with DS to initiate DNA replication.[7–9]

Maintenance of the oriP replicon is stable once EBV latency has been established. The loss rate of established oriP plasmids is estimated at 2–4% per cell generation.[10,11] Interestingly, the loss rate of the oriP replicon is significantly higher in cells transiently transduced with oriP plasmids (>25% per cell generation) than in established cells.[12] In primary B cells, EBV DNA is lost rapidly within 2 days post-infection (~98.9%).[13] However, the loss rate of the EBV genome during a week post-infection in B cells remains to be quantified.

Upon EBV infection, the first viral genes expressed are the transactivators EBNA2 and EBNA-LP transcribed from Wp several hours after infection.[7] EBNA2 binds to the EBNA2-responsive elements and, in cooperation with EBNA-LP, enhances transcription from Cp, which leads to expression of all EBNA proteins, including EBNA1. EBNA1 binding to oriP activates C/Wp to boost viral latent gene expression, including the EBNAs and LMP-1. The viral gene transactivation positive feedback loop is established within a few days post-infection, and EBNA1 is one of the key factors that sustain this feedback loop during the acute phase of EBV infection.[14] In parallel, EBNA1 contributes to the establishment of the EBV genome as a licensed replicon. It may be possible to stop EBV infection by breaking the chain of EBNA1-dependent events and thus the EBV-mediated malignant transformation of infected cells. Previous studies have assessed the therapeutic potential of a dominant-negative derivative of EBNA1 (dnE1) in cells in which EBV latency was already established.[15,16] In this study, we critically assessed whether inhibition of EBNA1 limits the early stage of EBV infection in B cells. We provide evidence that expression of dnE1 strongly blocks the expression of virus-encoded oncogenes in acutely infected cells without accelerating EBV genome loss, and disrupts EBV latency in the subacute phase of EBV infection.

Materials and Methods

Cells. The 293T, EBV-negative Burkitt lymphoma cell line BJAB, EBV-positive Burkitt lymphoma cell line Daudi, EBV-transformed healthy donor-derived B lymphoblastoid cell line (B-LCL), and B acute lymphoblastic leukemia cell line BALL-1

[4]To whom correspondence should be addressed.
E-mail: ajkomano@nih.go.jp

doi: 10.1111/j.1349-7006.2009.01474.x

cells (kindly provided by Dr. Yokota, National Institute of Infectious Diseases, Tokyo, Japan) were maintained in RPMI-1640 medium (Sigma, St. Louis, MA, USA) supplemented with 10% fetal bovine serum (Japan Bioserum, Tokyo, Japan), 50 U/mL penicillin, 50 μg/mL streptomycin (Invitrogen, Tokyo, Japan), and incubated at 37°C in a humidified 5% CO_2 atmosphere.

Plasmids. The following primers were used to amplify dnE1 from p1160[17] by PCR: 5′-ACCGGTCTCGAGCAATTGCCA-CCATGCGGGGTCAGGGTGATGGAGG-3′ and 5′-GGATC-CTCGAGCGGCCGCTCACTCCTGCCCTTCCTCACC-3′. The GFP-dnE1 expression vector (pGD) was constructed by cloning the MfeI-XhoI fragment of the PCR product into the BglII-SalI sites of pEGFP-C1 (Clontech, Palo Alto, CA, USA). The MfeI and BglII sites were blunted with T7 RNA polymerase. The AgeI-BamHI fragment from pGD was cloned into the corresponding restriction sites of pCMMP eGFP[15,18] to generate pCMMP GFP-dnE1. The EBNA1 expression vector p1553, the FR-tk-luciferase reporter p985, and pLuciferase (pCMV-luc) have been described previously.[17–20]

Luciferase assay. The 293T cells, grown in 48-well plates, were co-transfected with the indicated plasmids using Lipofectamine 2000 according to the manufacturer's protocol (Invitrogen, Tokyo, Japan). Cells were replated in 96-well plates in triplicate at 2 h post-transfection. Luciferase activity was measured 48 h after transfection using the Steady-Glo Kit (Promega, Madison, WI, USA).

Murine leukemia virus (MLV) vector infection and cell sorting. MLV vectors were produced as described previously.[18] B cells (1×10^7 cells) were incubated with 2 mL of MLV preparation overnight at 4°C with continuous agitation. GFP-positive cells were collected using a FACS sorter (FACS Vantage; Becton Dickinson, San Jose, CA, USA) at 11 days post-infection.

Western blotting. Western blotting was performed as described previously.[21,22] The following reagents were used: anti-GFP (MsX Green Fluorescent Protein; Chemicon, Temecula, CA, USA) and Envision$^+$ Dual Link System-HRP (Dako, Glostrup, Denmark).

EBV infection and nucleic acid extraction. The EBV B95-8 strain was a generous gift from Dr Fujiwara's group at the National Research Institute for Child and Development (Tokyo, Japan). B cells (1×10^7 cells) were incubated with 100 μL of B95-8 EBV for 1 h at 37°C, and genomic DNA was extracted from half of the infected cells soon after infection (QIAamp DNA Mini Kit; Qiagen, Tokyo, Japan). At 15 h post-infection, half of the cells were washed once with PBS and incubated for 5 min in lysis buffer (10 mM Tris-HCl [pH7.4], 10 mM NaCl, 3 mM $MgCl_2$, and 0.5% NP-40). The nuclear fraction was collected by centrifugation for 5 min at 20.6 K × *g* (Kubota 3740; Kubota, Tokyo, Japan), and high molecular weight DNA was extracted (nuclear DNA). At 2 days post-infection and at later time points, high molecular weight DNA, or total RNA (PureLink Total RNA Blood Purification Kit; Invitrogen) was extracted from 1×10^6 or 3×10^6 cells, respectively, according to the manufacturer's protocol. After EBV infection, 10 μM aciclovir (Kayaku, Tokyo, Japan) was added to the culture medium. The production and infection of the recombinant EBV Akata strain carrying GFP and neomycin resistant genes has been described previously.[23] At 2 days post-infection, cells were plated at a density of 1×10^4 cells per well in a flat-bottomed 96-well plate, and cultured in a medium containing 1 mg/mL G418. The efficiency of EBV latency establishment was evaluated as percentage of wells positive for the emergence of G418-resistant cells at 2 to 3 weeks post-G418 selection.

Quantitative real-time PCR. Real-time PCR was performed as described previously; serial dilutions of positive controls were used as standards.[21] Amplifications were performed using the QuantiTect SYBR Green RT-PCR/PCR Kit (Qiagen), and the following primers: BamHI W repeat, 5′-GCCAGAGG-TAAGTGGACTTT-3′ and 5′-AGAAGCATGTATACTAAGC-CTCCC-3′; cyclophilin A (CYPA), 5′-CACCGCCACCATG-GTCAACCCCA-3′ and 5′-CCCGGGCCTCGAGCTTTCGAG-TTGTCCACAGTCAGCAATGG-3′; C/Wp, 5′-CCCTCGGA-CAGCTCCTAAG-3′ and 5′-CTTCACTTCGGTCTCCCCTA-3′; EBER1, 5′-AAAACATGCGGACCACCAGC-3′ and 5′-AG-GACCTACGCTGCCCTAGA-3′. The β-globin primers were described previously.[21] Following PCR amplification, the amplicons were separated in a 2% agarose gel, stained with ethidium bromide, and imaged with a Typhoon scanner (GE Healthcare Bio-Sciences; Piscataway, NJ, USA).

Results

Construction and functional verification of dnE1 fused to GFP. The carboxy half of EBNA1 serves as a functional dominant-negative inhibitor of EBNA1 that restricts the replication and maintenance of oriP plasmids as well as the EBNA1-dependent enhancement of transcription.[17,24] We used a dnE1 mutant encompassing amino acids 377 to 391 (the nuclear localization signal, NLS) and 451 to 641 (the DNA binding and dimerization domain) of EBNA1 (Fig. 1A).[17] To visualize the intracellular distribution of dnE1, we constructed the retroviral expression vector encoding GFP-dnE1. The expression of GFP-dnE1 was verified in transiently transfected 293T cells and stably transduced B cell lines using an MLV vector. To verify the function of GFP-dnE1, we conducted a reporter assay using a plasmid encoding the FR-tk-luciferase cassette. EBNA1 enhances expression of FR-tk-luciferase by binding to FR. If the GFP-dnE1 construct retains dnE1 function, co-expressing EBNA1 and GFP-dnE1 should reduce reporter activity. Luciferase activity was increased significantly upon EBNA1 expression by approximately 5.3-fold, consistent with previous findings (Fig. 1B, $P < 0.05$, two-tailed Student's *t*-test).[17] When GFP-dnE1 was co-expressed, the luciferase activity was decreased. The decrease in luciferase activity was proportional to the increase in GFP-dnE1 expression vector (Fig. 1B, maximum reduction: 22.3%, $P < 0.05$, two-tailed Student's *t*-test). This effect was not observed with GFP alone. In addition, CMV promoter-driven luciferase expression was unaffected by EBNA1, GFP-dnE1, and GFP, suggesting that the reduction in luciferase activity with GFP-dnE1 in the EBNA1/FR-tk-luciferase system is specific. These data indicate that GFP-dnE1 functions as an inhibitor of EBNA1.

Establishment of B cells constitutively expressing GFP-dnE1. To investigate the potential effect of GFP-dnE1 on EBV infection in B cells, we established BALL-1 and BJAB cells, which constitutively express GFP-dnE1, using an MLV vector. GFP was used as a control throughout this study. The distribution of GFP-dnE1 was examined by confocal microscopy, which revealed an even distribution of GFP throughout the cell. In contrast, the majority of GFP-dnE1was localized to the nucleus due to the presence of the NLS (Fig. 2A). Similar observations were made in BJAB and 293T cells (data not shown). We sorted the GFP- or GFP-dnE-expressing cells using a FACS sorter. To test the dose-dependent effect, we collected BALL-1 cell populations bearing high or low levels of GFP fluorescence, denoted as Hi and Lo, respectively. The expression of GFP and GFP-dnE1 was verified by Western blotting, which confirmed that GFP and GFP-dnE1 Hi cells had higher intensity signals than the GFP and GFP-dnE1 Lo cells (Fig. 2B). The rate of cell proliferation and the morphology of GFP-dnE1 cells were indistinguishable from those of GFP cells (Fig. 2A and data not shown).

Effect of GFP-dnE1 on the nuclear translocation of EBV DNA during the acute phase of EBV infection. To assess whether GFP-dnE1 could restrict the nuclear targeting of the EBV

doi: 10.1111/j.1349-7006.2009.01474.x

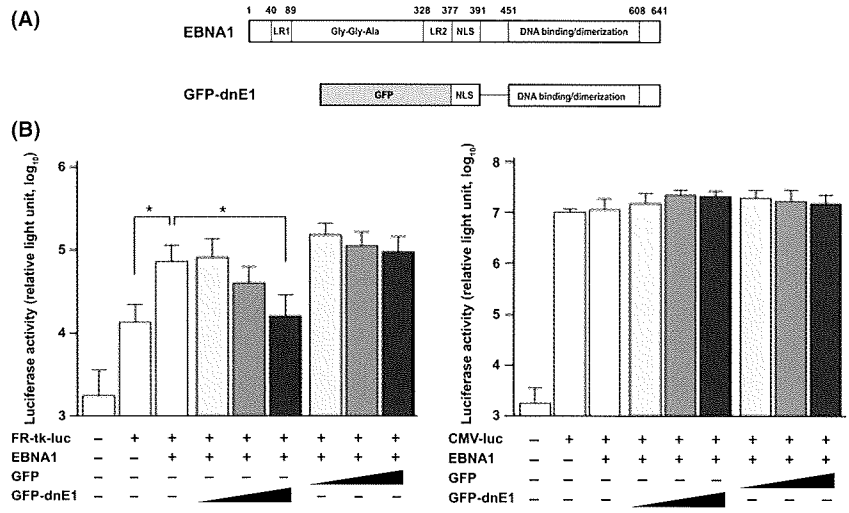

Fig. 1. Construction and functional characterization of a dominant-negative EBNA1 mutant (dnE1) fused to green fluorescent protein (GFP). (A) Structure of the EBNA1 protein and dnE1 used in this study. The linking regions (LR1 and LR2), the Gly-Gly-Ala repeat, the nuclear localization signal (NLS), and the DNA binding and dimerization domain are shown. GFP-dnE1 encodes the NLS and DNA binding and dimerization domain of EBNA1 fused to the C-terminus of GFP. (B) Repression of EBNA1-dependent transcriptional activation by GFP-dnE1. We transfected 293T cells in 48-well plates with 200 ng of FR-tk-luc or CMV-luc reporter, and 500 ng of EBNA1 expression vector, along with increasing amounts of GFP or GFP-dnE1 expression vector (20, 100, and 500 ng, respectively). *$P < 0.05$, two-tailed Student's *t*-test.

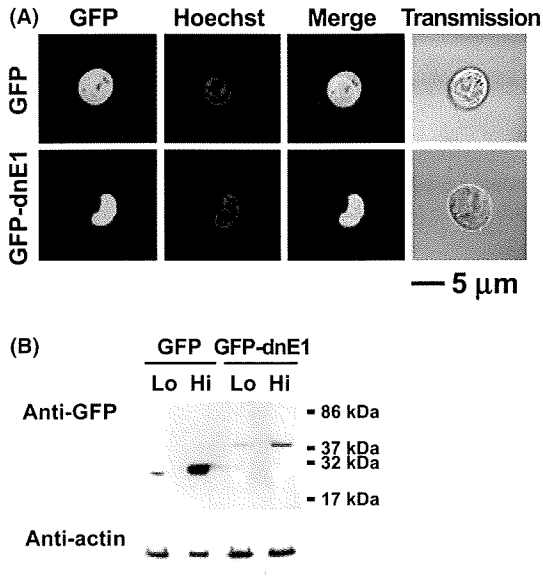

Fig. 2. Verification of stable green fluorescent protein (GFP)-dominant-negative EBNA1 (dnE1) expression in BALL-1 cells. (A) Distribution of GFP and GFP-dnE1 in BALL-1 cells was examined by confocal microscopy. Cells were imaged unfixed using a confocal microscope META 510 (Carl Zeiss, Tokyo, Japan). The green signal represents GFP fluorescence, and blue represents the Hoechst-stained nucleus. The bar represents 5 μm; magnification, ×630. (B) GFP or GFP-dnE1 expression in stably transduced BALL-1 cells was examined by Western blot analysis using an anti-GFP antibody. Protein lysates from 5×10^5 cells were loaded for each sample, except GFP Hi cells (5×10^4). The molecular weight marker is shown on the right.

genome after infection, we measured the amount of EBV DNA recovered from cells immediately after infection (representing the amount of EBV attached to cells) and the amount of EBV DNA that had migrated into the nucleus at 1 day post-infection. We isolated the nuclear fraction to exclude EBV DNA that failed to enter the nucleus. The number of EBV DNA molecules per cell was estimated by real-time PCR, which targeted the BamHI W repeat, in 10 ng of genomic DNA. We estimated the number of EBV DNA per cell given that a single cell contains approximately 10 pg of genomic DNA, and an EBV DNA has 10 copies of BamHI W repeats on average. The nuclear targeting efficiencies of EBV DNA were as follows: BALL-1 GFP cells, 43.3–108.6%; GFP-dnE1 cells, 46.9–65.6%; BJAB GFP cells, 37.4%; GFP-dnE1 cells, 35.0% (Table 1). These data suggested that the effect of GFP-dnE1 on the nuclear targeting of EBV DNA should be assessed more sensitively in BALL-1 and BJAB cell systems than in primary B cells because the nuclear targeting efficiency of EBV DNA in primary B cells is extremely inefficient (~1.1%).[13] In our experimental systems, the nuclear targeting efficiencies of EBV DNA in GFP-dnE1-expressing cells were similar to those in GFP-expressing cells. In addition, the dose-dependency of GFP-dnE1 was not observed in BALL-1 cells (Table 1). These data suggest that the nuclear targeting efficiency of EBV DNA was not restricted by the presence of GFP-dnE1 in B cells upon EBV infection.

Effect of GFP-dnE1 on the rate of loss of EBV DNA during the acute phase of EBV infection. To examine the effect of GFP-dnE1 on the rate of loss (ROL) of EBV DNA during the acute phase of viral infection, we monitored the EBV DNA copy number from day 2 to day 5 or day 6 post-infection, by real-time PCR, which detects the viral genome in both linear and circular configurations (Table 1). The ROL was estimated as the percentage reduction of EBV DNA per cell generation, considering that the cell doubling time is 24 h, and the kinetics of viral genome loss follows an exponential decay. The ROL in GFP-dnE1-expressing cells (19.2–85.9% per cell generation) was similar to GFP-expressing cells (20.5–79.4% per cell generation) in both BALL-1 and BJAB cells. In addition, there was no detectable dose-dependent effect of GFP-dnE1 in BALL-1 cells (Table 1 and Fig. 3). The averages ± SEs of ROL in GFP- and GFP-dnE1-expressing cells from six independent measurements in BALL-1 cells were 37.7 ± 10.7% and 25.7 ± 6.5% per cell generation, respectively (data not shown), which was substantially higher than the rate of loss of an established oriP replicon (2–4%).[10,11] These results reflect the precipitous loss of oriP plas-

Table 1. The kinetics of EBV DNA in the acute phase of EBV infection

Cell	Copy number of EBV DNA per cell at the indicated day†				Nuclear transport (%‡)	Rate of loss of EBV DNA (% per cell generation§)
Expt 1						
BALL-1	Day 0	Day 1	Day 2	Day 5		
GFP Hi	20.38	11.92	3.57	0.01¶	58.5	85.9
GFP Lo	17.26	11.68	3.21	0.56	67.7	44.1
GFP-dnE1 Hi	23.02	10.79	3.30	0.30	46.9	54.9
GFP-dnE1 Lo	18.83	12.36	1.46	0.53	65.6	28.7
BJAB	Day 0	Day 1	Day 2	Day 5		
GFP	155.1	58.8	5.38	0.06	37.4	77.7
GFP-dnE1	64.6	37.4	5.69	0.05	58.0	79.4
Expt 2						
BALL-1	Day 0	Day 1	Day 2	Day 6		
GFP Hi	16.33	17.73	11.10	4.74	108.6	19.2
GFP Lo	17.35	7.51	8.75	1.13	43.3	40.1
GFP-dnE1 Hi	18.46	8.71	8.95	3.38	47.2	21.6
GFP-dnE1 Lo	14.14	7.05	6.97	2.79	49.9	20.5

†Nuclear DNA was used for day 1 data. ‡Estimated from day 0 and day 1 data. §Estimated from day 2 and day 5 or day 6 data with the exponential decay. ¶Below the limit of detection. dnE1, dominant-negative EBNA1; EBV, Epstein–Barr virus; GFP, green fluorescent protein.

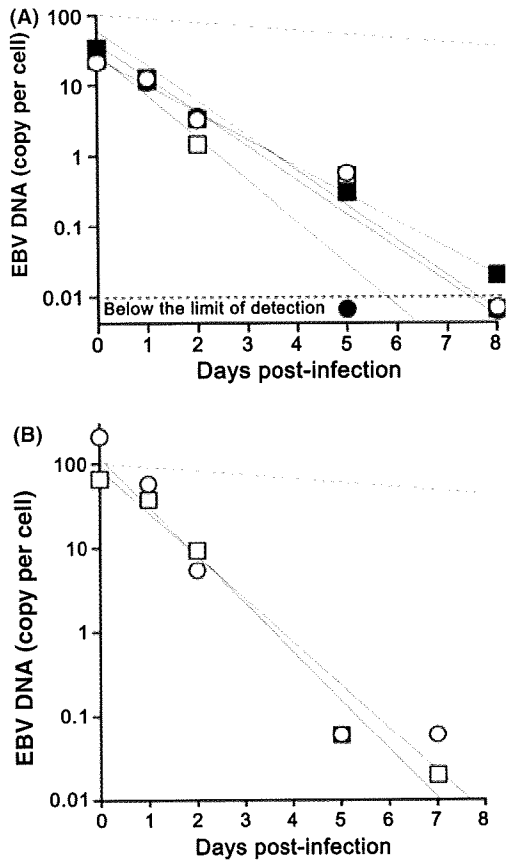

Fig. 3. Kinetics of Epstein–Barr virus (EBV) DNA loss during the acute phase of EBV infection. (A) Representative data from BALL-1 cells (Expt. 1 in Table 1) is shown. The filled squares, open squares, filled circles, and open circles represent GFP Hi, GFP Lo, GFP-dnE1 Hi, and GFP-dnE1 Lo, respectively. The limit of detection was below 0.01 (dashed line). The gray lines represent an approximation to the exponential decay. The dashed gray line represents the 4% rate of loss per cell generation. (B) Representative data from BJAB cells shown in Table 1. The circles and squares represent GFP and GFP-dnE1, respectively. Please see Table 1 for the detailed analysis.

mids (26–37%) in transiently transfected non-B cells.[12] The data suggest that GFP-dnE1 is unable to accelerate the ROL in the acute phase of EBV infection in B cells, presumably because the EBV genome is not established as an EBNA1-dependent stable licensed replicon. It should be noted that this is the first time that quantitative ROL data has been obtained by introducing the oriP replicon into B cells via EBV infection, which is an approach that does not confer any selective advantage on the infected cells.

Effect of GFP-dnE1 on efficiency of establishment of EBV latency. Cells infected with recombinant EBV, carrying the neomycin resistance gene, were seeded at 5×10^3 cells per well into a 96-well plate, and the efficiency of the establishment of EBV latency was assessed as the percentage of wells positive for the emergence of G418-resistant cells. G418-resistant cells appeared in BJAB, Daudi, parental BALL-1, and BALL-1 GFP cells at 56–100% efficiencies. In sharp contrast, G418-resistant cells were absent from GFP-dnE1-expressing BALL-1 cells (Table 2). These data clearly suggest that, although the ROL during the acute phase of EBV infection was not enhanced by GFP-dnE1, GFP-dnE1 was able to block the establishment of EBV latency completely during the subacute phase of EBV infection.

Effect of GFP-dnE1 on EBV-encoded latent gene expression. EBV gene expression was tested at 2 days post-infection by quantitative RT-PCR. We focused on the C/Wp activity because it expresses key viral transactivators including EBNA1, -2, -3s, and -LP to boost viral transforming gene expression. We detected C/Wp-driven transcripts in GFP Hi BALL-1 cells as expected. Conversely, C/Wp-driven transcripts were undetectable in GFP-dnE1 Hi and Lo BALL-1 cells, although these cells retained similar EBV DNA levels to GFP-expressing cells (Fig. 4 and Table 3). The Cp-driven transcript was under the limit of detection by RT-PCR, suggesting that the Wp is predominantly activated at the early phase of EBV infection consistent with previous findings.[7] Inhibition of viral gene transcription was not observed in the RNA polymerase III-driven transcript EBER1,[25] and cyclophilin A mRNA levels were similar between GFP- and GFP-dnE1-expressing cells (Fig. 4 and Table 3). This indicates that the effect of GFP-dnE1 on C/Wp activity is specific, and uncovers an active role of EBNA1 in supporting transactiva-

doi: 10.1111/j.1349-7006.2009.01474.x

Table 2. The establishment efficiency of EBV latency

Cell	Emergence of G418-resistant cells†	
BJAB	100%	(6/6)
Daudi	100%	(10/10)
BALL-1		
Parental	56%	(5/9)
GFP Hi	67%	(2/3)
GFP-dnE1 Hi	0%	(0/6)
GFP-dnE1 Lo	0%	(0/6)

†Percentage of wells positive for G418-resistant cells over the number of tested wells from 96-well plates indicated in the bracket. Shown are the sum of two independent experiments. dnE1, dominant-negative EBNA1; EBV, Epstein–Barr virus; GFP, green fluorescent protein.

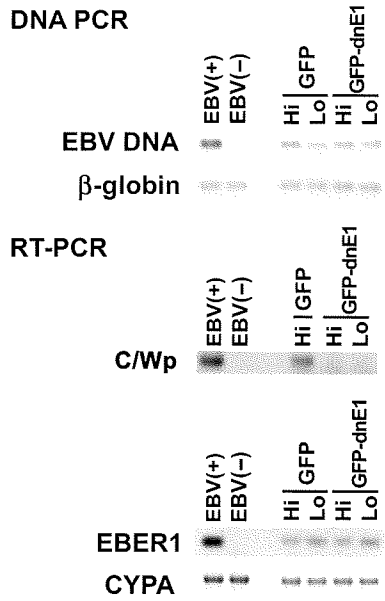

Fig. 4. PCR-based analysis of Epstein–Barr virus (EBV) gene expression. The effect of green fluorescent protein (GFP)-dominant-negative EBNA1 (dnE1) on the loss of EBV DNA (DNA PCR, upper panels) and transcription of the C/W promoter-driven transcript (C/Wp), EBER1, and cyclophilin A (CYPA; RT-PCR, lower panels) in BALL-1 cells at 2 days post-infection were examined. EBV-transformed B-lymphoblastoid cell line (B-LCL) and BJAB cells, denoted as EBV(+) and EBV(–), were used as positive and negative controls for viral DNA and RNA shown, respectively. β-Globin and CYPA were used as controls.

Table 3. Quantification of EBV transcripts in BALL-1 cells by real-time PCR at 2 days post-infection

BALL-1 cells		W1/2 exon (copies†)	EBER1 (copies‡)	CYPA (copies‡)
GFP	Hi	2.2	2.8×10^2	1.4×10^6
	Lo	NT§	0.8×10^2	1.0×10^6
GFP-dnE1	Hi	BLD¶	3.3×10^2	1.3×10^6
	Lo	BLD¶	1.2×10^2	1.5×10^6

†Copies per 13–14 ng total cellular RNA. ‡Copies per 200 ng total cellular RNA. §Not tested. ¶Below the limit of detection. CYPA, cyclophilin A; dnE1, dominant-negative EBNA1; EBV, Epstein–Barr virus; GFP, green fluorescent protein.

tion from C/Wp. Taken together, these results show that inhibition of EBNA1 functions strongly restricts EBV-encoded transforming gene expression and, although there is no detectable effect on the ROL of EBV DNA at the acute phase of viral infection, it blocks the establishment of EBV latency during the subacute phase.

Discussion

This is the first report describing the effect of EBNA1 inhibition from the onset of EBV infection in B cells. Unexpectedly, the dnE1 was unable to accelerate the ROL during the acute phase of EBV infection since dnE1 enhanced the loss of the oriP plasmid in the transient transfection assays.[10,11] In the subacute phase of EBV infection, the establishment of EBV latency was potently blocked by dnE1. In addition, we observed a strong repressive effect of dnE1 on the EBNA1-dependent enhancement of viral gene transcription from C/Wp during the early phase of EBV infection, similar to the transient transfection assays.[17] These data suggest that viral oncogene expression depends heavily on EBNA1 during the acute phase of viral infection, and that EBNA1 contributes little to EBV genome maintenance during this period. The results emphasize that an EBNA1 inhibitor should serve as an attenuator of viral oncogene expression since activation of C/Wp is the 'root' event of the positive feedback loop involved in the transactivation of viral transforming gene expression. In this regard, the EBNA1 inhibition approach could be superior to LMP-1 or EBNA2 inhibition.

If EBNA1 binding to oriP is essential for both the enhancement of viral gene transcription and for genome maintenance, what mechanism prevents dnE1 from affecting the ROL during the acute phase of EBV infection? It is likely that maintenance of the oriP replicon immediately after its introduction into cells is less efficient than in cells harboring an 'established' oriP replicon as an autonomously replicating plasmid. The ROL of an established oriP replicon is 2–4% per cell generation.[10,11] In contrast, our data from the EBV/B cell-based assay gave an average ROL of 26–38% during the week post-infection (acute phase of EBV infection). In agreement with our findings, it is reported that a transiently transduced oriP replicon is lost from cells at 26–37% per cell generation 1–2 weeks post-plasmid transduction.[12] These data indicate that maintenance of the oriP replicon is largely EBNA1-independent immediately after its introduction into cells, regardless of whether the route of introduction is by transfection or EBV infection. In other words, the establishment of EBV latency should be a rare epigenetic event. The data also suggest that the artificial minichromosome approach may be relevant in understanding EBV genome behavior.[12]

Our study suggests that gene therapy using GFP-dnE1 is an attractive approach, not only for therapeutics, but also for prophylactic interventions of EBV-associated malignancies. For example, in peripheral blood stem cell transplantation (PBSCT), GFP-dnE1 transduction into $CD34^+$ cells should protect the differentiated B cells from EBV infection, thus preventing the genesis of EBV-associated B cell lymphomas. We will attempt to prove this hypothesis using a small animal model in future studies.[26] Additionally, EBNA1 is a potential molecular target for developing a small molecular-weight EBV inhibitor as mentioned previously.[14,15] The advantages of EBNA1-inhibitor development are that the biological assay system is already established and the X-ray crystal structure of the DNA-bound EBNA1 DNA binding and dimerization domain is known, which means that computer-aided drug design technology can be immediately applied. Although EBV is associated with various malignancies, preventive and therapeutic measures against EBV infection have not been developed. We believe that an anti-EBV agent, such as an EBNA1 inhibitor, would have an enormous impact in the medical field due to the substantial number of patients with EBV-associated malignancies.

Acknowledgments

We thank Drs Kenichi Imadome and Shigeyoshi Fujiwara for reagents. We also thank Dr Bill Sugden for critically reading the manuscript. This work was supported by the Japan Health Science Foundation, the Ministry of Health, Labor and Welfare of Japan, and the Ministry of Education, Culture, Sports, Science and Technology of Japan.

Disclosure Statement

The authors have no conflict of interest.

References

1 Thompson MP, Kurzrock R. Epstein–Barr virus and cancer. *Clin Cancer Res* 2004; **10**: 803–21.
2 Rickinson AB, Kieff E. Epstin–Barr virus. In: Knipe DM, Howley PM, eds. *Fields Virology*, 5th edn, vol. 2. Philadelphia: Lippincott Williams & Wilkins, 2007; 2655–700.
3 Klein E, Kis LL, Klein G. Epstein–Barr virus infection in humans: from harmless to life endangering virus-lymphocyte interactions. *Oncogene* 2007; **26**: 1297–305.
4 Snow AL, Martinez OM. Epstein–Barr virus: evasive maneuvers in the development of PTLD. *Am J Transplant* 2007; **7**: 271–7.
5 Besson C, Goubar A, Gabarre J *et al.* Changes in AIDS-related lymphoma since the era of highly active antiretroviral therapy. *Blood* 2001; **98**: 2339–44.
6 Carbone A, Cesarman E, Spina M, Gloghini A, Schulz TF. HIV-associated lymphomas and gamma-herpesviruses. *Blood* 2009; **113**: 1213–24.
7 Kieff E, Rickinson AB. Epstin–Barr virus and its replication. In: Knipe DM, Howley PM, eds. *Fields Virology*, 5th edn, vol. 2. Philadelphia: Lippincott Williams & Wilkins, 2007; 2603–54.
8 Lindner SE, Sugden B. The plasmid replicon of Epstein–Barr virus: mechanistic insights into efficient, licensed, extrachromosomal replication in human cells. *Plasmid* 2007; **58**: 1–12.
9 Wang J, Sugden B. Origins of bidirectional replication of Epstein–Barr virus: models for understanding mammalian origins of DNA synthesis. *J Cell Biochem* 2005; **94**: 247–56.
10 Kirchmaier AL, Sugden B. Plasmid maintenance of derivatives of oriP of Epstein–Barr virus. *J Virol* 1995; **69**: 1280–3.
11 Sugden B, Warren N. Plasmid origin of replication of Epstein–Barr virus, oriP, does not limit replication in cis. *Mol Biol Med* 1988; **5**: 85–94.
12 Leight ER, Sugden B. Establishment of an oriP replicon is dependent upon an infrequent, epigenetic event. *Mol Cell Biol* 2001; **21**: 4149–61.
13 Hurley EA, Thorley-Lawson DA. B cell activation and the establishment of Epstein–Barr virus latency. *J Exp Med* 1988; **168**: 2059–75.
14 Altmann M, Pich D, Ruiss R, Wang J, Sugden B, Hammerschmidt W. Transcriptional activation by EBV nuclear antigen 1 is essential for the expression of EBV's transforming genes. *Proc Natl Acad Sci U S A* 2006; **103**: 14188–93.
15 Kennedy G, Komano J, Sugden B. Epstein–Barr virus provides a survival factor to Burkitt's lymphomas. *Proc Natl Acad Sci U S A* 2003; **100**: 14269–74.
16 Nasimuzzaman M, Kuroda M, Dohno S *et al.* Eradication of Epstein–Barr virus episome and associated inhibition of infected tumor cell growth by adenovirus vector-mediated transduction of dominant-negative EBNA1. *Mol Ther* 2005; **11**: 578–90.
17 Kirchmaier AL, Sugden B. Dominant-negative inhibitors of EBNA-1 of Epstein–Barr virus. *J Virol* 1997; **71**: 1766–75.
18 Komano J, Miyauchi K, Matsuda Z, Yamamoto N. Inhibiting the Arp2/3 complex limits infection of both intracellular mature vaccinia virus and primate lentiviruses. *Mol Biol Cell* 2004; **15**: 5197–207.
19 Aiyar A, Sugden B. Fusions between Epstein–Barr viral nuclear antigen-1 of Epstein–Barr virus and the large T-antigen of simian virus 40 replicate their cognate origins. *J Biol Chem* 1998; **273**: 33073–81.
20 Middleton T, Sugden B. EBNA1 can link the enhancer element to the initiator element of the Epstein–Barr virus plasmid origin of DNA replication. *J Virol* 1992; **66**: 489–95.
21 Urano E, Kariya Y, Futahashi Y *et al.* Identification of the P-TEFb complex-interacting domain of Brd4 as an inhibitor of HIV-1 replication by functional cDNA library screening in MT-4 cells. *FEBS Lett* 2008; **582**: 4053–8.
22 Shimizu S, Urano E, Futahashi Y *et al.* Inhibiting lentiviral replication by HEXIM1, a cellular negative regulator of the CDK9/cyclin T complex. *AIDS* 2007; **21**: 575–82.
23 Kanda T, Yajima M, Ahsan N, Tanaka M, Takada K. Production of high-titer Epstein–Barr virus recombinants derived from Akata cells by using a bacterial artificial chromosome system. *J Virol* 2004; **78**: 7004–15.
24 Mackey D, Sugden B. The linking regions of EBNA1 are essential for its support of replication and transcription. *Mol Cell Biol* 1999; **19**: 3349–59.
25 Howe JG, Shu MD. Epstein–Barr virus small RNA (EBER) genes: unique transcription units that combine RNA polymerase II and III promoter elements. *Cell* 1989; **57**: 825–34.
26 Yajima M, Imadome K, Nakagawa A *et al.* A new humanized mouse model of Epstein–Barr virus infection that reproduces persistent infection, lymphoproliferative disorder, and cell-mediated and humoral immune responses. *J Infect Dis* 2008; **198**: 673–82.

doi: 10.1111/j.1349-7006.2009.01474.x

A New Humanized Mouse Model of Epstein-Barr Virus Infection That Reproduces Persistent Infection, Lymphoproliferative Disorder, and Cell-Mediated and Humoral Immune Responses

Misako Yajima,[1,a] Ken-Ichi Imadome,[1,a] Atsuko Nakagawa,[2] Satoru Watanabe,[3] Kazuo Terashima,[4] Hiroyuki Nakamura,[1] Mamoru Ito,[6] Norio Shimizu,[3] Mitsuo Honda,[5] Naoki Yamamoto,[4,5] and Shigeyoshi Fujiwara[1]

[1]Department of Infectious Diseases, National Research Institute for Child Health and Development, [2]Pathology Laboratory, Department of Clinical Laboratory Medicine, National Center for Child Health and Development, [3]Department of Virology, Division of Medical Science, Medical Research Institute, and [4]Department of Molecular Virology, Graduate School of Medicine, Tokyo Medical and Dental University, and [5]AIDS Research Center, National Institute of Infectious Diseases, Tokyo, and [6]Central Institute for Experimental Animals, Kawasaki, Japan

The functional human immune system, including T, B, and natural killer lymphocytes, is reconstituted in NOD/Shi-*scid*/IL-2Rγ^{null} (NOG) mice that receive hematopoietic stem cell transplants. Here, we show that these humanized mice can recapitulate key aspects of Epstein-Barr virus (EBV) infection in humans. Inoculation with $\sim 1 \times 10^3$ TD_{50} (50% transforming dose) of EBV caused B cell lymphoproliferative disorder, with histopathological findings and latent EBV gene expression remarkably similar to that in immunocompromised patients. Inoculation with a low dose of virus ($\leqq 1 \times 10^1$ TD_{50}), in contrast, resulted in apparently asymptomatic persistent infection. Levels of activated $CD8^+$ T cells increased dramatically in the peripheral blood of infected mice, and enzyme-linked immunospot assay and flow cytometry demonstrated an EBV-specific T cell response. Immunoglobulin M antibody specific to the EBV-encoded protein BFRF3 was detected in serum from infected mice. The NOG mouse is the most comprehensive small-animal model of EBV infection described to date and should facilitate studies of the pathogenesis, prevention, and treatment of EBV infection.

Epstein-Barr virus (EBV) is a tumor virus associated with a variety of malignancies, including Burkitt lymphoma, nasopharyngeal carcinoma, and Hodgkin lymphoma [1]. It is also an etiological agent of infectious mononucleosis (IM), which is characterized by transient proliferation of EBV-infected B lymphoblastoid cells and an excessive anti-EBV T cell response. EBV has a unique ability to growth transform human B lymphocytes in vitro and establish lymphoblastoid cell lines (LCLs) [2]. EBV-transformed lymphoblasts express 6 nuclear proteins (Epstein-Barr nuclear antigen [EBNA] 1, 2, 3A, 3B, 3C, and LP) and 3 membrane proteins (latent membrane protein [LMP] 1, 2A, and 2B), and this pattern of EBV gene expression is termed latency III. In contrast, Burkitt lymphoma cells express only EBNA1 consistently (latency I), whereas Hodgkin lymphoma and nasopharyngeal carcinoma cells express EBNA1, LMP1, and LMP2 (latency II). In vivo, EBV-transformed cells are effectively removed by virus-specific cytotoxic T cells, and EBV infection in immunocompetent humans is usually subclinical, except for IM caused by primary infection during adolescence or adulthood. However, in immunocompromised hosts, such as patients with AIDS and transplant recipients, EBV-infected B lymphoblasts can proliferate and cause lymphoproliferative disorder.

Received 28 December 2007; accepted 19 March 2008; electronically published 15 July 2008.

Potential conflicts of interest: none reported.

Financial support: Ministry of Health, Labour, and Welfare of Japan (grants H18-Shinko-013 and H19-AIDS-003).

[a] M.Y. and K.-I.I. contributed equally to this study.

Reprints or correspondence: Dr. Shigeyoshi Fujiwara, Dept. of Infectious Diseases, National Research Institute for Child Health and Development, 2-10-1 Okura, Setagaya-ku, Tokyo 157-8535, Japan (shige@nch.go.jp); or, Dr. Norio Shimizu, Dept. of Virology, Div. of Medical Science, Medical Research Institute, Tokyo Medical and Dental University, 1-5-45 Yushima, Bunkyo-ku, Tokyo 113-8519, Japan (nshivir@tmd.ac.jp); or, Dr. Naoki Yamamoto, AIDS Research Center, National Institute of Infectious Diseases, 1-23-1 Toyama, Shinjuku-ku, Tokyo 162-8640, Japan (nyama@nih.go.jp).

The Journal of Infectious Diseases 2008; 198:673–82

0022-1899/2008/19805-0008$15.00

DOI: 10.1086/590502

EBV infects only humans in nature and limited animal species under experimental conditions. It can infect cotton-top tamarins and induce lymphomas, which have been used as a model of EBV-associated lymphomas [3, 4]. Nonhuman primates possess their own lymphocryptoviruses related to EBV, and research on the use of these virus-host systems as models of EBV infection is currently in progress [5, 6]. Small-animal models of EBV have also been developed, which are particularly useful when a large number of animals are necessary. *Scid* mice that receive intraperitoneal transplants of EBV-transformed LCLs or peripheral blood mononuclear cells (PBMCs) isolated from EBV-infected persons develop lymphomas, which have been used as a model of human lymphoproliferative disorder [7–9]. Recently, NOD/*scid* mice transplanted with human hematopoietic stem cells (HSCs) and reconstituted mainly with B lymphocytes were infected with EBV, and the development of lymphoproliferative disorder was described [10]. The immune response to EBV was not studied in these *scid* or NOD/*scid* mouse models. Very recently, a functional human immune system could be reconstituted in highly immunodeficient mouse strains, and these so-called humanized mice were shown able to mount an EBV-specific T cell response [11, 12]. These studies were, however, performed mainly using immunological standpoints and did not provide detailed virological data.

NOD/Shi-*scid*/IL-2Rγ^{null} (referred to here as NOG) is a highly immunodeficient mouse strain that was developed very recently and that, after transplantation with cord blood HSCs, is able to reconstitute most major components of the hematolymphoid system, including T cells, B cells, NK cells, macrophages, and dendritic cells [13–15]. Human T cells that develop in NOG mice are functional in that they can be activated to display cytotoxic activity [15, 16]. These properties made NOG mice an excellent model of human virus infections targeting the immune system, such as those with human T-lymphotropic virus–1 and HIV-1 [17–20]. Here, we provide evidence that humanized NOG mice can reproduce various key aspects of human EBV infection and propose that they may be a valuable tool for studies of EBV infection.

METHODS

Preparation of humanized mice. NOG mice were obtained from the Central Institute for Experimental Animals (Kawasaki, Japan). Protocols for experiments with NOG mice were approved by the Institutional Animal Care and Use Committee of the National Institute of Infectious Diseases (NIID). Cord blood was supplied by the Tokyo Cord Blood Bank after obtaining informed consent. The use of human materials in this research was approved by the institutional review boards of the National Research Institute for Child Health and Development, the NIID, the Tokyo Medical and Dental University, and the Tokyo Cord Blood Bank. The isolation of human $CD34^+$ HSCs from cord blood by means of the MACS Direct CD34 Progenitor Cell Isolation Kit (Miltenyi Biotec), their intravenous injection (1×10^4 to 1.2×10^5 cells/mouse) into 6–10-week-old female NOG mice, and the characterization of the reconstitution of the human hematoimmune system were done as described elsewhere [18, 20]. NOG mice in which the human hematoimmune system was reconstituted are referred here as humanized NOG (hNOG) mice.

Table 1. Primers for reverse-transcription polymerase chain reaction to detect Epstein-Barr virus (EBV) transcripts.

Transcript, primer	Sequence (5'→3')
EBNA1	
5'	gatgagcgtttgggagagctgattctgca
3'	tcctcgtccatggttatcac
EBNA2	
5'	agaggaggtggtaagcggttc
3'	tgacgggtttccaagactatcc
LMP1	
5'	ctctccttctcctcctcttg
3'	caggagggtgatcatcagta
LMP2A	
5'	atgactcatctcaacacata
3'	catgttaggcaaattgcaaa
LMP2B	
5'	cagtgtaatctgcacaaaga
3'	catgttaggcaaattgcaaa
EBER1	
5'	agcacctacgctgccctaga
3'	aaaacatgcggaccaccagc
BZLF1 (first)	
5'	attgcaccttgccgccaccttg
3'	cgcattttctggaagccacccga
BZLF1 (second)	
5'	gaccaagctaccagagtctat
3'	cagaatcgcattcctccagcga
BMRF1	
5'	ctagccgtcctgtccaagtgc
3'	agccaaacagctccttgccca
BLLF1	
5'	gtcagtacaccatccagagcc
3'	ttggtagacagccttcgtatg
GAPDH	
5'	gcctcctgcaccaccaactg
3'	cgacgcctgcttcaccaccctct

NOTE. EBNA, Epstein-Barr nuclear antigen; EBER, EBV-encoded small RNA; LMP, latent membrane protein.

Experimental EBV infection, quantification of viral DNA, and detection of viral mRNAs. Virus production by EBV-infected Akata cells was stimulated by brief treatment with anti-IgG antibody (Dako), and culture fluid was used as inoculum after filtration through a 0.45-μm membrane filter [21]. For virus titration, cord blood lymphocytes were plated at the density

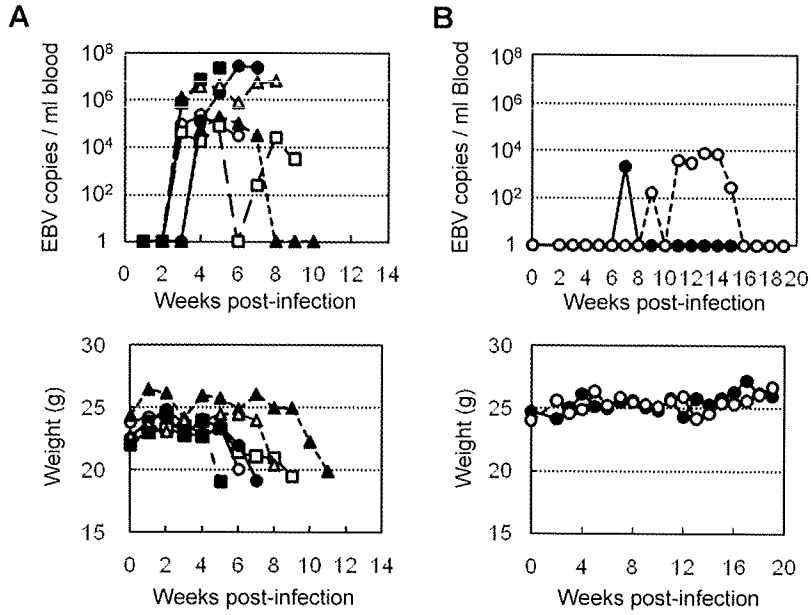

Figure 1. Peripheral blood Epstein-Barr virus (EBV) DNA load and body weight in humanized NOG (hNOG) mice infected with EBV. *A,* Infection at a high dose of virus. Six mice were inoculated intravenously with 1×10^3 TD_{50} of EBV. Peripheral blood EBV DNA load *(upper panels)* and body weight *(lower panels)* were then determined weekly. Each symbol in the graphs represents an individual mouse. Interruption of records indicates the death or killing of a mouse. *B,* Infection at lower doses. Peripheral blood EBV DNA load *(upper panel)* and body weight *(lower panel)* of 2 mice inoculated with low doses of EBV (*black circle,* 1×10^{-1} TD_{50}; *white circle,* 1×10^1 TD_{50}) are shown.

of 2×10^5 cells per well in 6-well plates and then inoculated with serial 10-fold dilutions of virus preparation. The number of wells with proliferating lymphocytes was counted 6 weeks after infection, and the titer of the virus in 50% transforming dose (TD_{50}) was determined by the Reed-Muench method [22]. EBV was inoculated intravenously through the tail vein. EBV DNA was quantified by a real-time quantitative polymerase chain reaction (PCR) assay based on the TaqMan system (Applied Biosystems), as described elsewhere [23]. Analysis of EBV gene expression by reverse-transcription PCR (RT-PCR) was done as described elsewhere, using the primers listed in table 1 [24].

Histopathology, in situ hybridization (ISH), and immunohistochemistry. Tissue samples were fixed in 10% buffered formalin, embedded in paraffin, and stained with hematoxylin-eosin. For phenotypic analysis of proliferating lymphocytes, immunostaining for CD3 (Nichirei), CD4 (Novocastra), CD8 (Nichirei), CD45RO, CD20, CD79a, CD30, Mum1 (Dako), CD23, CD10, CD56 (Novocastra), granzyme B (Dako), and T cell intracellular antigen 1 (Beckman Coulter) was performed on paraffin sections. EBV was detected by immunostaining for LMP1 and EBNA2 (Dako) and by ISH with EBV-encoded small RNA (EBER) probe. Immunohistochemistry and ISH were performed on an automated stainer (Benchmark XT; Ventana Medical Systems), in accordance with the manufacturer's recommendations. To determine the cell lineage of EBV-infected cells, paraffin sections were applied to double staining with EBER ISH and immunohistochemistry.

Detection of EBV-specific T cell response. Enzyme-linked immunospot (ELISPOT) assay was performed with the Immunocyto IFN-γ ELISPOT Kit (MBL), in accordance with the instructions supplied by the manufacturer. Briefly, $CD8^+$ T cells were isolated from PBMCs from EBV-infected hNOG mice with the IMag anti-human CD8 Particles–DM (BD Biosciences). Mixture of these $CD8^+$ T cells and an autologous LCL were incubated with interleukin (IL)–2 in microplates coated with antibody to interferon (IFN)–γ for 17 h. Captured IFN-γ was detected by use of biotinated antibody to IFN-γ and alkaline phosphatase–conjugated streptavidin and was visualized by reaction with the BCIP/NBT chromogen substrate. The unpaired Student's *t* test was used for statistical analysis. IFN-γ secretion in response to EBV was also examined by flow cytometry, as described elsewhere [25]. Briefly, aliquots of murine splenocytes and an LCL were mixed in 6-well plates in the presence of brefeldin A (10 μg/mL) and incubated at 37°C in 5% CO_2 for 17 h. After incubation, the cell suspensions were stained with phycoerythrin-conjugated anti-human CD69, phycoerythrin–Texas red–conjugated anti-human CD45, and phycoerythrin–cyanin 5–conjugated anti-human CD8 for 30 min at 4°C and were fixed with 2% paraformaldehyde. Cells were then permeabilized and stained with BD Perm/Wash buffer (BD Biosciences) containing fluorescein isothiocyanate–conjugated anti-human IFN-γ for 30 min at 4°C. Stained cells were analyzed using an EpicsXL flow cytometer (Beckman Coulter).

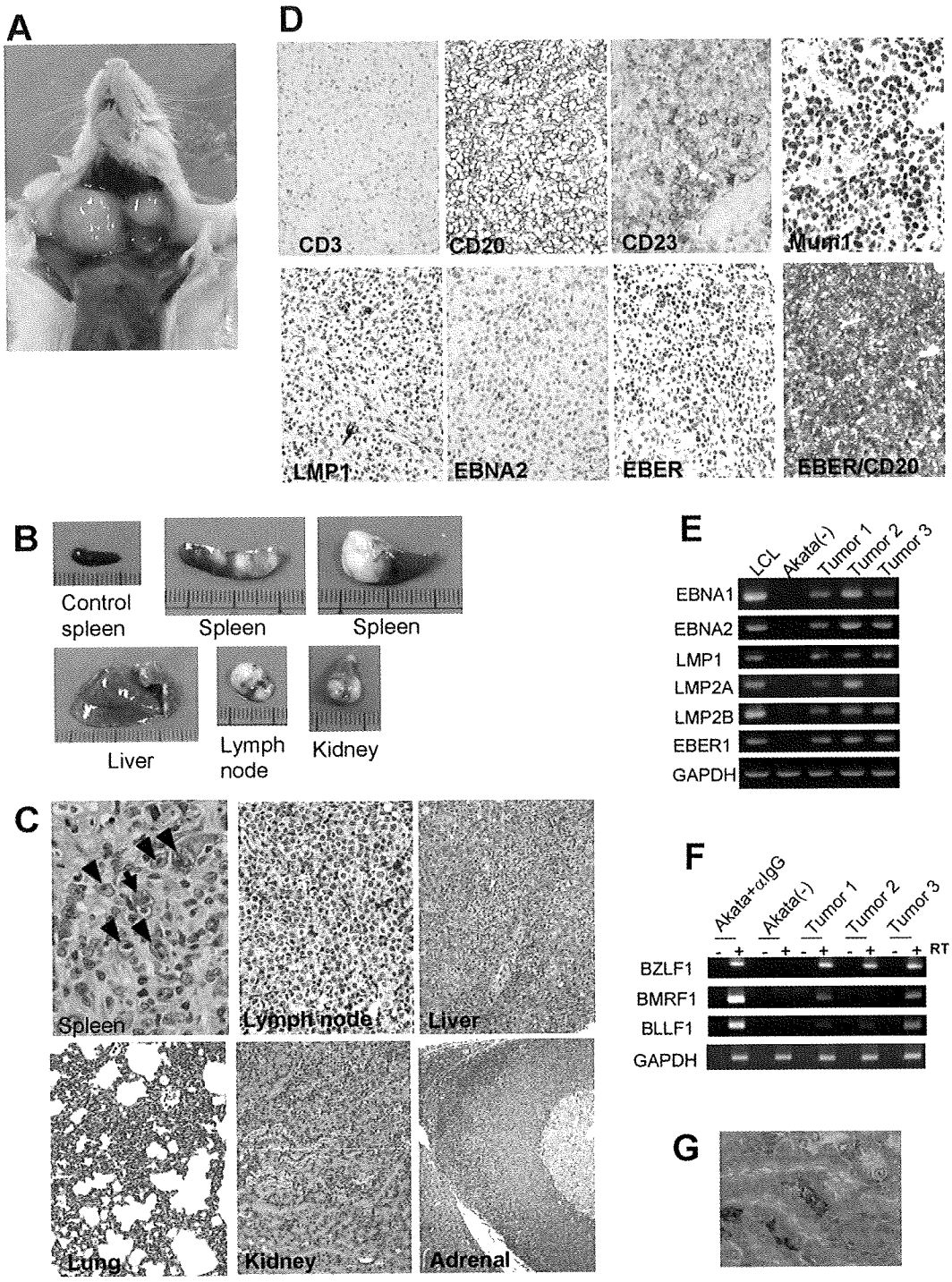

Figure 2. Pathological and virological analyses of Epstein-Barr virus (EBV)–infected humanized NOG (hNOG) mice. *A,* Photograph of an EBV-infected mouse showing tumors in the cervical area. *B,* Photographs of spleens, liver, lymph node, and kidney from EBV-infected mice with lymphoproliferative disorder. The upper left panel shows the spleen from an uninfected mouse. *C,* Photomicrographs of hematoxylin-eosin–stained tissues from mice with lymphoproliferative disorder. The arrow indicates a Reed-Sternberg–like cell, and the arrowheads indicate Hodgkin-like cells. Original magnifications, ×1000 for spleen, ×400 for lymph node, and ×200 for liver, lung, kidney, and adrenal gland. *D,* Immunohistochemical staining for lymphocyte surface markers (CD3, CD20, CD23, and Mum1) and EBV-encoded proteins (latent membrane protein [LMP] 1 and Epstein-Barr nuclear antigen [EBNA] 2), as well as in situ hybridization for EBV-encoded small RNA (EBER), in a lymph node from a mouse with lymphoproliferative disorder. The bottom right panel represents double staining for EBER and CD20. Original magnifications, ×200 for all except EBER/CD20, which is ×400. *E* and *F,* Reverse-transcription polymerase chain reaction detection of latent-cycle *(E)* and lytic-cycle *(F)* EBV gene expression in tumors from EBV-infected hNOG mice. Spleen tumors from 3 different mice were examined for the expression of EBNA1, EBNA2, LMP1, LMP2A, LMP2B, EBER1, BZLF1, BMRF1, and BLLF1. RNA samples from a lymphoblastoid cell line (LCL) *(E)* and anti-IgG–treated Akata cells *(F)* were used as positive controls, and an RNA sample from EBV-negative Akata cells (*E* and *F*) was used as a negative control. Assays were done with (+) or without (−) reverse transcriptase (RT) in panel F. Expression of GAPDH was examined as a reference. *G,* Double staining of EBER and CD20 in the liver of an hNOG mouse that was persistently infected with EBV without developing lymphoproliferative disorder. EBER is stained navy in the nucleus, and CD20 is stained brown in the membrane. Original magnification, ×1000.

Table 2. Quantification of Epstein-Barr virus (EBV) DNA in persistently infected humanized NOG mice.

Organ	Mouse	
	N35-1[a]	N35-3[b]
Bone marrow	ND	4.1×10^4
Spleen	6.2×10^2	5.7×10^3
Liver	ND	2.7×10^4
Lymph node (neck)	1.6×10^3	6.9×10^3
Lymph node (axilla)	ND	2.6×10^2
Lymph node (mesentery)	ND	4.1×10^2
Lungs	2.7×10^3	1.0×10^4
Kidneys	1.2×10^3	4.8×10^4
Adrenal gland	4.4×10^1	8.0×10^5

NOTE. Data are the amounts of EBV DNA measured 22 weeks after infection, in copies per microgram of DNA. ND, not detectable.

[a] Infected at 1×10^{-1} TD_{50}.

[b] Infected at 1×10^1 TD_{50}.

Detection of antibodies specific to EBV. IgM antibody to the EBV BFRF3 protein was detected by immunoblotting essentially as described elsewhere [24], except that horseradish peroxidase–conjugated antibody specific to human IgM (Beckman Coulter) was used as secondary antibody. To prepare the glutathione *s*-transferase (GST)–BFRF3 fusion protein, a DNA fragment spanning the entire coding region of BFRF3 was amplified by PCR (sense primer, 5'-GGCTCGAATTCATGGCACGCCGGCTGCCC-3'; antisense primer, 5'-GGCTCGGATCCATACACCATGTTTCGTGCCC-3') and inserted to the GST fusion vector pSGENT2, to yield the plasmid pSGENT2-BFRF3. *Escherichia coli* cells harboring pSGENT2-BFRF3 were stimulated with isopropyl β-D-1-thiogalactopyranoside to induce the expression of GST-BFRF3, which was subsequently purified by use of the Bulk GST Purification Module (GE Healthcare).

RESULTS

EBV infection in hNOG mice. Transplantation of human $CD34^+$ HSCs in NOG mice and reconstitution of the human hematoimmune system were done as described elsewhere [18, 20]. In the initial attempts at infection, 1×10^3 TD_{50} of the Akata strain of EBV was inoculated into 6 hNOG mice, and EBV DNA was demonstrated in the peripheral blood of all of them (figure 1*A*). EBV DNA was first evident at 3–4 weeks after inoculation and reached peak levels of $\sim 1 \times 10^6$ EBV DNA copies/μg of DNA. All 6 mice became seriously ill between 5 and 10 weeks after inoculation, with signs of weight loss (figure 1*A*), general inactivity, and piloerection. In contrast, EBV DNA was not detected in the peripheral blood, bone marrow, thymus, spleen, lymph nodes, liver, kidneys, and lungs of 3 control NOG mice that were not transplanted with HSCs but were inoculated with the virus (data not shown). Similarly, no signs of EBV infection were observed in 3 control hNOG mice that were not inoculated with the virus (data not shown). In total, 43 NOG mice that had been humanized with HSCs from 9 different cord blood samples were inoculated with 1×10^3 TD_{50} of EBV, and in 38 of them the results were similar to those observed in the initial 6 mice, with high blood EBV load and severe deterioration in their general condition. Ten of them died and could not be examined further. The remaining 28 mice were killed, and signs of lymphoproliferative disorder were found at autopsy (see the below). These results demonstrate that hNOG mice can be infected with EBV, with a mostly fatal outcome at this virus dose.

EBV-induced lymphoproliferative disorder in hNOG mice. Autopsy of killed mice showed signs of lymphoproliferative disorder typically represented by an overt tumor in the spleen (figure 2*B*). In ~70% (20/28) of the mice autopsied, macroscopical signs of disseminated disease were found in the liver, lymph nodes, or kidneys (figure 2*A* and 2*B*). Seventeen mice were examined pathologically, and 15 of them showed typical histology of diffuse large B cell lymphoma, with remarkable similarity to the human lymphoproliferative disorder in the immunocompromised hosts (figure 2*C*). The tissues contained occasional immunoblasts, Reed-Sternberg–like cells, and Hodgkin-like cells (figure 2*C*). Marked infiltration of large transformed lymphoid cells was also demonstrated in liver, lymph nodes, kidneys, adrenal glands, and lungs (figure 2*C*). Real-time PCR detected high levels ($\sim 1 \times 10^5$ to $\sim 1 \times 10^6$ EBV DNA copies/μg of DNA) of EBV DNA in these organs, and the large transformed lymphoid cells were universally EBV positive by EBER ISH (figure 2*D*). Immunohistochemical analysis showed that the large transformed lymphoid cells were of the activated B cell phenotype, being reactive for CD20 and CD23 and not reactive for CD3 and CD10 (figure 2*D* and data not shown). They were also positive for Mum-1, a late- and postgerminal center cell marker. The EBER-positive cells were CD20-positive B cells (figure 2*D*), and no EBER-positive T cells were identified. Immunostaining revealed that most proliferating cells expressed EBNA2, whereas LMP1 was expressed in only a fraction of them (figure 2*D*). RT-PCR analysis of typical spleen tumors obtained from 3 different mice showed the expression of EBNA1, EBNA2, LMP1, LMP2A, LMP2B; and EBER, consistent with the latency III program of EBV gene expression (figure 2*E*). In addition, transcripts from lytic-cycle EBV genes, including BZLF1 (immediate-early), BMRF1 (early), and BLLF1 (late, encoding gp350/220), were identified (figure 2*F*).

Virus dose–dependent outcome of EBV infection in hNOG mice. To examine the influence of virus dose on the outcome of EBV infection, we inoculated serial dilutions of EBV preparation into 2 lots of hNOG mice, each consisting of 5 mice that had been humanized with the same HSC preparation. Consistent with the results described above, the 4 mice (2 from each lot) that received the higher doses (1×10^3 and 1×10^2 TD_{50}) of the

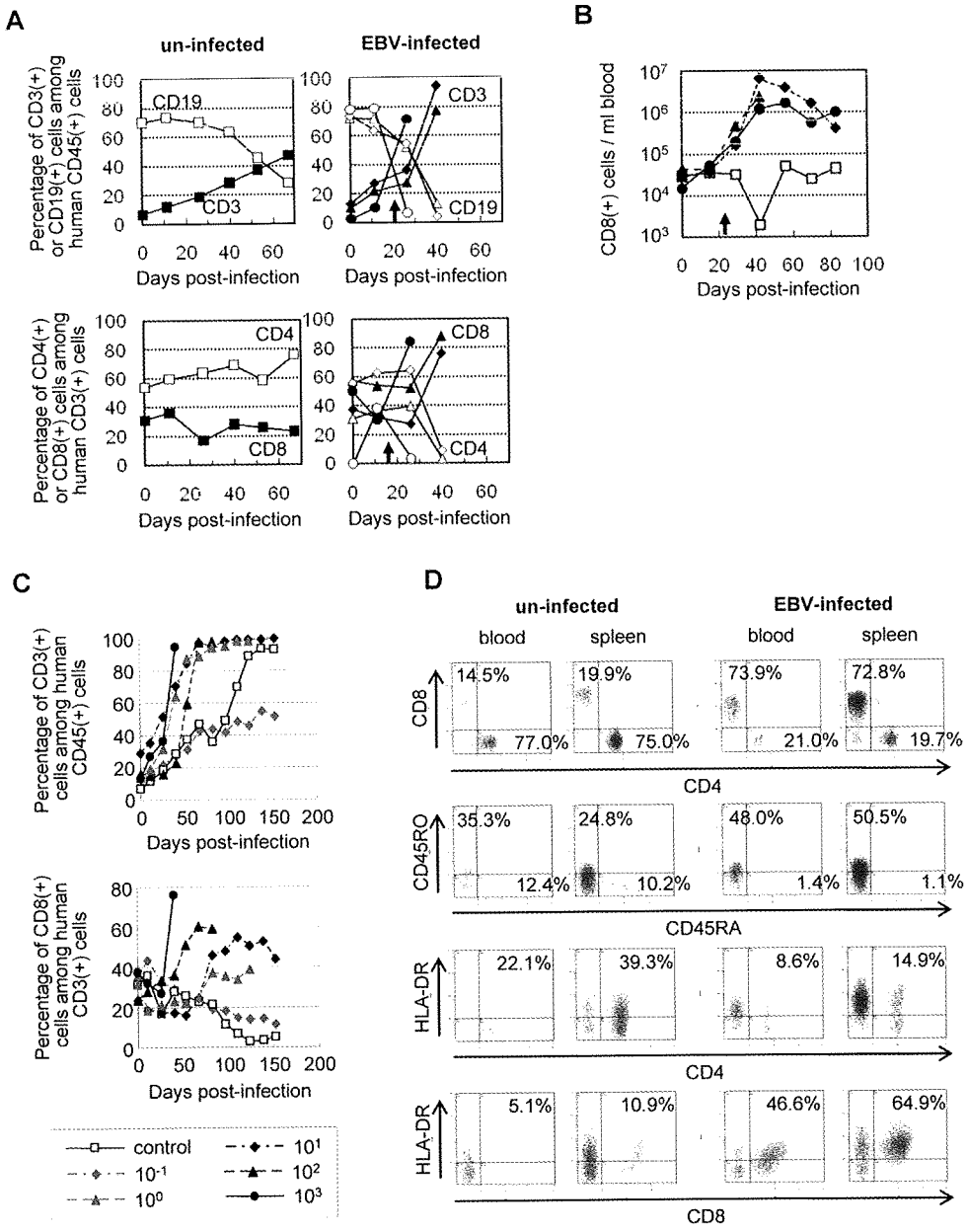

Figure 3. Surface marker expression by peripheral blood T cells in Epstein-Barr virus (EBV)–infected humanized NOG (hNOG) mice. *A,* Changes in the percentages of $CD3^+$ T cells and $CD19^+$ B cells among human $CD45^+$ leukocytes *(upper panels)* and in the percentages of $CD8^+$ cells and $CD4^+$ cells among $CD3^+$ cells *(lower panels)* after infection with EBV. Results obtained from 3 EBV-infected mice and an uninfected mice are shown. White symbols indicate the percentage of $CD19^+$ cells *(upper panels)* or $CD4^+$ cells *(lower panels);* black symbols indicate the percentage of $CD3^+$ cells *(upper panels)* or $CD8^+$ cells *(lower panels).* A vertical arrow in the graph area shows the time point at which EBV DNA was first detected in peripheral blood. *B,* Changes in the no. of $CD8^+$ T cells in the peripheral blood of EBV-infected hNOG mice. White symbols indicate uninfected mice, and black symbols indicate infected mice. Note that cell no. is plotted in a logarithmic scale. *C,* Viral dose–dependent T cell responses in hNOG mice inoculated with serially diluted EBV. Ten-fold serial dilutions of an EBV sample starting from 1×10^3 TD_{50} per inoculate were injected intravenously into NOG mice that had undergone transplantation with the same lot of human hematopoietic stem cells (HSCs). Changes in the percentages of $CD3^+$ T cells among human $CD45^+$ leukocytes *(upper panel)* and in the percentages of $CD8^+$ cells among $CD3^+$ cells *(lower panel)* after inoculation with EBV are shown. The viral dose for each mouse is shown in the key. *D,* Comparison of surface marker expression between EBV-infected mice and control mice. Two mice that underwent transplantation with the same lot of human HSCs were either inoculated with EBV or left uninfected; 10 weeks after inoculation, mononuclear cells obtained from peripheral blood or spleen were gated for the expression of human CD3 and then examined for the expression of CD8 and CD4 *(top panels),* CD45RO and CD45RA *(second from top),* HLA-DR and CD4 *(second from bottom),* and HLA-DR and CD8 *(bottom).*

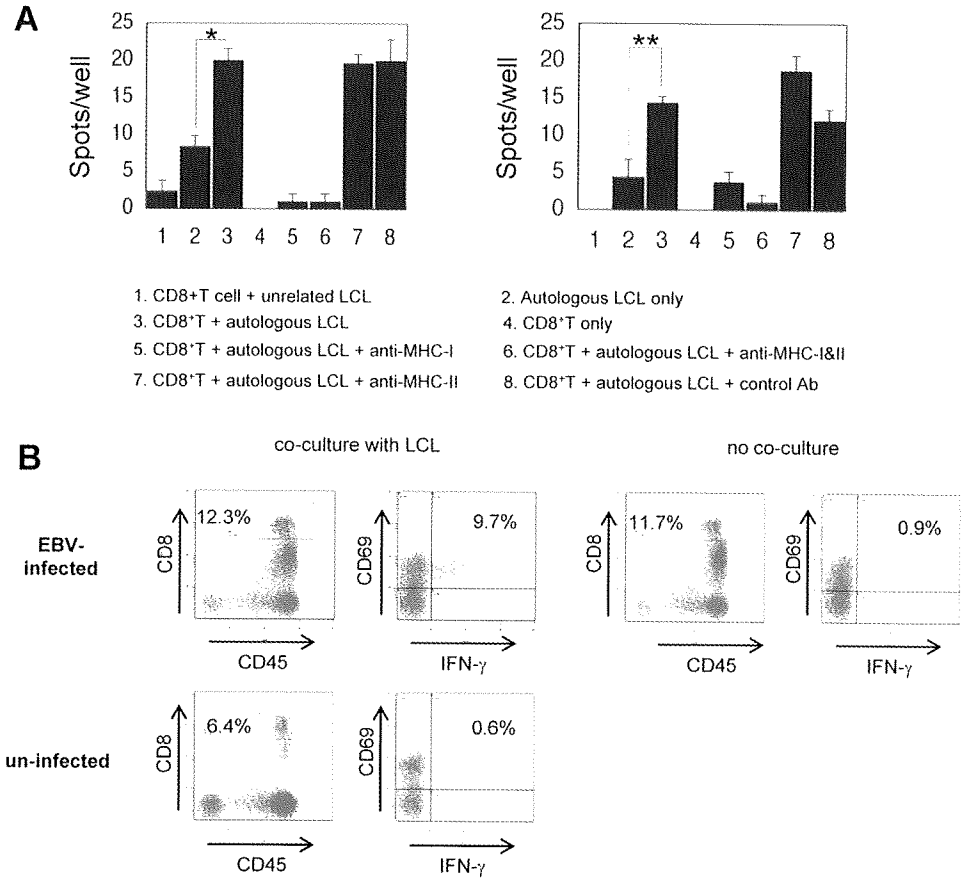

Figure 4. Epstein-Barr virus (EBV)–specific T cell response in humanized NOG (hNOG) mice. *A*, Enzyme-linked immunospot assay for the detection of human T cells producing interferon (IFN)–γ after stimulation with an EBV-positive lymphoblastoid cell line (LCL). $CD8^+$ cells isolated from EBV-infected hNOG mice were cocultured with an autologous LCL, and IFN-γ–secreting cells were counted (3, 5, 6, 7, and 8). To analyze restriction by major histocompatibility complex (MHC), antibody to HLA class I (anti–human HLA-ABC clone W6/32; eBioscience) (5), antibodies to both HLA class I and class II (6), antibody to HLA class II (anti–human HLA-DP,DQ,DR clone CR3/43; Dako) (7), or isotype-matched control antibody (8) were added to the culture. Control experiments included coculture of $CD8^+$ cells with an MHC-mismatched LCL (1), culture of the autologous LCL only (2), and culture of $CD8^+$ cells only (4). Results from 2 infected mice are shown. Five hundred $CD8^+$ cells per well were cultured in the experiment shown on the left, and 250 $CD8^+$ cells per well were cultured in that shown on the right. Spots were counted in triplicate in each of the 8 experimental groups, and the bars represent mean values and SEs. The unpaired Student's *t* test was used for statistical analysis. $^*P < .01$ and $^{**}P < .02$. *B*, Detection of human $CD8^+$ cells that produce IFN-γ in response to stimulation with an EBV-positive LCL by flow cytometry. $CD8^+$ cells were isolated from the spleen of an EBV-infected mouse and cocultured with the autologous LCL. Intracellular IFN-γ was stained and analyzed as described in Methods.

virus died of lymphoproliferative disorder ~5–10 weeks after inoculation. The remaining mice in both of the lots that received lower doses (1×10^1, 1×10^0, and 1×10^{-1} TD_{50}) survived acute infection and appeared normal throughout the observation period of 22 weeks. Although EBV DNA was detected at variable levels in their peripheral blood several weeks after inoculation, it returned to undetectable levels thereafter (figure 1*B*), suggesting that a certain protection mechanism worked to control EBV infection. Importantly, EBV DNA could be still detected in various organs, including spleen, liver, lungs, kidneys, and adrenal glands, at the end of the observation period (22 weeks), indicating that EBV persisted in these mice (table 2). Double staining for EBER and CD20 showed that EBV persisted in B cells (figure 2*G*). Macroscopical examination by autopsy at the end of the observation period did not reveal abnormality in these mice, except for moderate splenomegaly found in a mouse that received 1×10^1 TD_{50}. These results indicate that the outcome of EBV infection in hNOG mice varies with the virus dose; high doses of virus tend to cause fatal lymphoproliferative disorder, whereas lower doses induce apparently asymptomatic persistent infection.

EBV-specific T cell response in hNOG mice. Flow cytometry analysis demonstrated a dramatic increase in the percentage of $CD3^+$ T cells among the human $CD45^+$ leukocytes after infection with EBV. This increase in T cells was accompanied by an increase in the percentage of $CD8^+$ cells among human $CD3^+$ T cells. These changes were seen in virtually all infected mice, and the results from 3 mice are shown in figure 3*A*. The slow increase in the percentage of $CD3^+$ cells in the uninfected mouse represents the process of humanization (i.e., the development of hu-

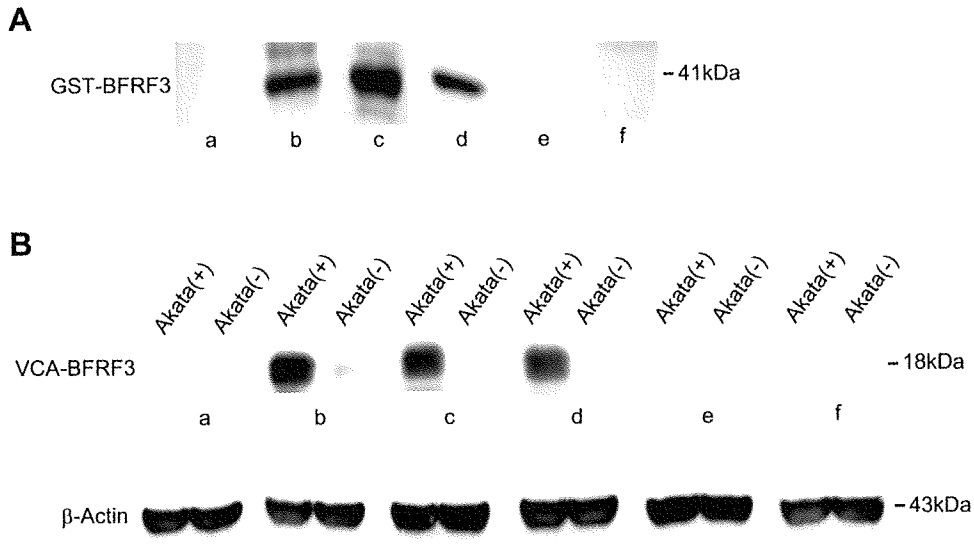

Figure 5. Demonstration of IgM antibody to the Epstein-Barr virus (EBV) BFRF3 protein in the serum of humanized NOG (hNOG) mice. *A*, Immunoblot with the glutathione *s*-transferase (GST)–BFRF3 fusion protein. Purified GST-BFRF3 fusion protein was examined with serum from an EBV-uninfected person *(a)*, an EBV-infected person *(b)*, EBV-infected hNOG mice (*c* and *d*), and an uninfected hNOG mice (*e* and *f*). *B*, Immunoblot with the lysate of EBV-producing Akata cells. Lysate of anti-IgG–treated Akata cells, labeled Akata(+), and of EBV-negative Akata cells, labeled Akata(−), was examined using serum from an EBV-uninfected person *(a)*, an EBV-infected person *(b)*, EBV-infected hNOG mice (*c* and *d*), and uninfected hNOG mice (*e* and *f*).

man T cells). This increase in $CD8^+$ cells were even more conspicuous when their definite number was counted (figure 3*B*). When hNOG mice were inoculated with serially diluted virus samples, a striking dose response was evident; mice inoculated with higher doses exhibited a more profound increase in $CD8^+$ cells at earlier time points (figure 3*C*). Further flow cytometry analyses showed that $CD45RO^+$ memory T cells, compared with $CD45RA^+$ T cells, increased in infected hNOG mice (figure 3*D*). Expression of a T cell activation marker, HLA-DR, was observed mainly in $CD8^+$ cells rather than in $CD4^+$ cells (figure 3*D*).

To demonstrate that these $CD8^+$ T cells were directed against EBV-infected cells, we examined IFN-γ secretion after stimulation with EBV-transformed cells. For this purpose, we first established an LCL using B cells isolated from the same cord blood that was used to isolate HSCs for transplantation. $CD8^+$ T cells, isolated from the peripheral blood of EBV-infected hNOG mice, were incubated with this autologous LCL, and cells secreting IFN-γ were detected by ELISPOT assay. For all 3 EBV-infected hNOG mice (which had been infected at 1×10^3 TD_{50}) thus examined, a significant number of spots were recognized in the wells in which $CD8^+$ T cells were mixed with the autologous LCL, whereas those cells incubated with unrelated LCL had many fewer spots (data from 2 mice are shown in figure 4*A*). $CD8^+$ T cells isolated from uninfected hNOG mice did not give a significant number of spots (data not shown). Release of IFN-γ was blocked by antibody specific to human major histocompatibility complex (MHC) class I but not by that specific to human MHC class II (figure 4*A*). These results clearly show that a T cell response restricted by human MHC class I was mounted against EBV-infected cells. In addition, in 5 of the 6 EBV-infected hNOG mice examined (infected at 1×10^3 TD_{50}), flow cytometry also demonstrated production of IFN-γ by $CD8^+$ T cells isolated from the spleen and stimulated with an autologous LCL (figure 4*B*).

EBV-specific antibody response in hNOG mice. Serum samples from 30 EBV-infected hNOG mice were examined by Western blotting for IgM antibodies reactive with a bacterially expressed GST-BFRF3 fusion protein. The BFRF3 protein is a major component of the virus capsid antigen of EBV [26]. The results are shown in figure 5*A* and indicated that four serum samples (from mice infected at 1×10^1 or 1×10^3 TD_{50}) contained IgM antibody reactive with it. These serum samples reacted also with the 18-kDa BFRF3-encoded protein in the lysate of Akata cells stimulated with IgG antibody to activate virus production (figure 5*B*). Similar experiments with human IgG–specific secondary antibody did not show a positive reaction with either GST-BFRF or $p18^{BFRF3}$. Six serum samples collected from uninfected hNOG mice reacted with neither the 18-kDa protein nor GST-BFRF3 (figure 5 and data not shown). These results indicate that hNOG mice have the ability to mount an IgM response to EBV.

DISCUSSION

The lymphoproliferative disease induced in hNOG mice is remarkably similar to the human lymphoproliferative disorder seen in immunocompromised hosts [27] with respect to histology, surface phenotype, and the type of EBV gene expression